HAL open science

Coupling finite elements of class C1 on composite curved meshes for second order elliptic problems

Ashish Bhole, Hervé Guillard, Boniface Nkonga, Francesca Rapetti

To cite this version:

Ashish Bhole, Hervé Guillard, Boniface Nkonga, Francesca Rapetti. Coupling finite elements of class C1 on composite curved meshes for second order elliptic problems. International Journal for Numerical Methods in Fluids, 2023, 10.1002/fld.5241 . hal-03913143

HAL Id: hal-03913143

https://hal.science/hal-03913143v1

Submitted on 26 Dec 2022

HAL is a multi-disciplinary open access archive for the deposit and dissemination of scientific research documents, whether they are published or not. The documents may come from teaching and research institutions in France or abroad, or from public or private research centers.

L'archive ouverte pluridisciplinaire **HAL**, est destinée au dépôt et à la diffusion de documents scientifiques de niveau recherche, publiés ou non, émanant des établissements d'enseignement et de recherche français ou étrangers, des laboratoires publics ou privés.

Received: Added at production | Revised: Added at production | Accepted: Added at production

DOI: xxx/xxxx

ARTICLE TYPE

Coupling finite elements of class C1 on composite curved meshes for second order elliptic problems

Ashish Bhole[1] | Hervé Guillard[1] | Boniface Nkonga[2] | Francesca Rapetti[2]

[1]CASTOR Project Team, Centre Inria, Rte des Luciolles, BP 93 06092 Sophia-Antipolis, France
[2]Département de Mathématiques, Université Côte d'Azur, Parc Valrose, 06108 Nice, France

Correspondence
*F. Rapetti Email: frapetti@unice.fr

Summary

Finite elements of class $\mathcal{C}^1$ are suitable for the computation of magnetohydrodynamics instabilities in tokamak plasmas. In addition, isoparametric approximations allow for a precise alignment of the mesh with the magnetic field line. Mesh alignment is crucial to achieve axisymmetric equilibria accurately. It is also helpful to deal with the anisotropy nature of magnetized plasma flows. In this numerical framework, several practical simulations are now available. They help to understand better the operation of existing devices and predict the optimal strategies for using the international ITER tokamak under construction. However, a mesh-aligned isoparametric representation suffers from the presence of critical points of the magnetic field (magnetic axis, X-point). We here explore a strategy that combines aligned mesh out of the critical points with non-aligned unstructured mesh in a region containing these points. By this strategy, we can avoid highly stretched elements and the numerical difficulties that come with them. The mesh-aligned interpolation uses bi-cubic Hemite-Bézier polynomials on a structured mesh of curved quadrangular elements. On the other hand, we assume reduced cubic Hsieh-Clough-Tocher finite elements on an unstructured triangular mesh. Both meshes overlap, and the resulting formulation is a coupled discrete problem solved iteratively by a suitable one-level Schwarz algorithm. In this paper, we will focus on the Poisson problem on a two-dimensional bounded regular domain. This elliptic equation is a simplified version of the axisymmetric tokamak equilibrium one at the asymptotic limit of infinite major radius (large aspect ratio).

KEYWORDS:
Composite meshes, isoparametric finite elements, reduced Hsieh-Clough-Tocher finite elements, Hermite-Bézier finite elements, alternating Schwarz method.

1 | INTRODUCTION

Magnetohydrodynamics instabilities play a critical role in magnetic confinement fusion power plants. Therefore, accurate numerical simulations are essential to investigate, avoid or mitigate the undesired consequences of destabilizing plasma equilibrium. For example, in tokamak devices, the balanced status of the Lorentz force and the pressure gradient is often axisymmetric and described by the Grad-Shafranov equation[1]. It is a highly nonlinear elliptic equation for the evolution of the poloidal magnetic flux in a two-dimensional cross-section of the tokamak[2]. Therefore, for simulating magnetohydrodynamics instabilities, it is desirable to have a strategy that preserves the equilibrium states without perturbations (the so-called well-balanced schemes)[3]. Furthermore, the evolution of strongly magnetized plasmas contains highly anisotropic patterns. Therefore, meshes aligned on the equilibrium magnetic flux lines, associated with an isoparametric finite element formulation, offer decisive advantages. The bi-cubic Hermite-Bézier[4] elements make for an accurate description of the magnetic topology using flux-aligned grids. In addition, the use of this kind of grid is particularly important to control artificial diffusion perpendicular to the flux surfaces. In this numerical framework, several practical simulations are now available. They help to understand better the operation of existing devices and predict the optimal strategies for using the international ITER tokamaks under construction[5,6].

However, at the critical points of the magnetic field (extrema or saddle points), finite element interpolation for aligned meshes has some drawbacks. Indeed, closed concentric flux lines at the plasma core make the aligned grid isomorphic to a polar grid. Hence, the geometric singularity at the symmetry center gives rise to several stretched elements[7]. Recently, in curved bi-cubic Hermite-Bézier interpolation, we have overcome the singularity at the magnetic axis (polar axis) by a proper linear combination of basis functions[8]. Nevertheless, this solution does not cure the presence of stretched elements and the method suffers from a loss of accuracy. Therefore, it seems reasonable to use a non-aligned unstructured grid associated with a $\mathcal{C}^1$ finite element locally near the magnetic axis. Unstructured grids fail for mesh alignment with the magnetic flux but avoid geometrical singularities and offer more flexibility in meshing complex geometries, local refinement, etc., while preserving accuracy.

Composite grid techniques are generally used by computational engineers in many large-scale simulations as a way to reduce the cost of grid generation (see, for example,[9]). Here, we will explore the possibility of combining two overlapping meshes, one of curved quadrangular pieces and the other of straight triangular elements, to tackle with the magnetic field critical points. Isoparametric bi-cubic Hermite-Bézier finite elements are adopted on the curved mesh and piece-wise cubic reduced Hsieh-Clough-Tocher ones are involved on the latter. As a first investigation, we consider the Laplace problem on a bounded domain D with regular boundary ∂D and Dirichlet type conditions on it. The continuity of the numerical solution in the region of overlap is enforced by interpolation. A one-level Schwarz algorithm is used to solve the coupled problem resulting from having adopted different spaces of finite elements in the subdomains.

The rest of the paper is organized as follows[1]. We start by stating in Section 2 the problem and its domain decomposition formulation in the continuous setting. In Section 3, we briefly recall the reduced Hsieh-Clough-Tocher element [10] on triangles and, taking the cue from [4], we present in detail the main steps for the isoparametric bi-cubic Hermite-Bézier one. We are then able to state the discrete coupled problem in Section 4 together with the one-level Schwartz algorithm for its solution. After the analysis of the algorithm convergence, we conclude in Section 5 with some numerical results.

2 | SETTING UP THE MODEL PROBLEM.

In an open bounded domain $D \subset \mathbb{R}^2$ with boundary ∂D, we consider the elliptic problem

$$\begin{aligned} \mathcal{L}\, u &= f \quad \text{in } D, \\ u &= g \quad \text{on } \partial D, \end{aligned} \tag{1}$$

for given functions f, g. For simplicity, the operator $\mathcal{L}$ is (minus) the Laplacian, $-\Delta$. The right-hand side $f \in L^2(D)$ with $L^2(D)$ the functional space of measurable functions on D that are square integrable in D, with norm $\|.\|_D^2$ associated with the scalar product $(v,w)_D = \int_D v\, w$. Let $H^1(D) = \{u \in L^2(D),\ \nabla u \in L^2(D)^2\}$ be the Hilbert space endowed with the semi-norm $|u|_{H^1(D)} = \|\nabla u\|_D$ and norm $\|u\|_{H^1(D)}^2 = \|u\|_D^2 + |u|_{H^1(D)}^2$. We assume that ∂D is piece-wise $\mathcal{C}^1$, so that the trace operator $u \mapsto u_{|\partial D}$ is continuous from $H^1(D)$ to $L^2(\partial D)$. We can hence take the boundary data g in $L^2(\partial D)$. To apply a Galerkin approach to problem (1) with $\mathcal{L} = -\Delta$, we consider its weak form: given $\tilde{u} \in H^1(D)$ with $\tilde{u}_{|\partial D} = g$, find $u \in H^1(D)$ such that $u - \tilde{u} \in H_0^1(\Omega)$ and

$$a_D(u,v) \ := \int_D \nabla u \cdot \nabla v = \int_D f\, v \ =: (f,v)_D \qquad \forall\, v \in H_0^1(D), \tag{2}$$

where $H_0^1(D) = \{v \in H^1(D),\ v_{|\partial D} = 0\}$.

We now introduce the domain decomposition framework. Let $\omega \subset D$ be a sub-domain of D with boundary $\gamma = \partial\omega$ and such that $\omega \cap \partial D = \emptyset$ (as in Fig. 1, left-side). We denote by Ω the complement of ω in D, that is $\Omega = D \setminus \bar{\omega}$. Note that the function $\tilde{u} \in H^1(D)$ is then selected to take zero value in $\overline{\omega}$. To formulate (2) in a domain decomposition framework, let us introduce the functional space

$$\mathcal{V} = \{(v,w) \in H^1(\Omega) \times H^1(\omega), \quad v_{|\gamma} = w_{|\gamma}\}.$$

The weak form (2) becomes: find $(u_\Omega, u_\omega) \in \mathcal{V}$ such that $u_\Omega - \tilde{u} \in H_0^1(\Omega)$ and

$$\mathsf{a}((u_\Omega, v), (u_\omega, w)) := a_\Omega(u_\Omega, v) + a_\omega(u_\omega, w) = \ell((v,w)), \qquad \forall\, (v,w) \in \mathcal{V}_0, \tag{3}$$

with $\ell((v,w)) = (f_{|\Omega}, v)_\Omega + (f_{|\omega}, w)_\omega$. The bilinear form $a_D(.,.)$ is continuous and elliptic on $\mathcal{V}_0$. In fact, the continuity of $a_D(.,.)$ on the space $\mathcal{V}_0$ results straightforwardly from the Cauchy-Schwarz inequality and its ellipticity is a direct consequence of the Poincaré inequality.

[1] Abbreviations: Degrees of freedom (dofs), Hermite-Bézier (HB), reduced Hsieh-Clough-Tocher (rHCT), Finite elements (FEs).

Thus problem (3) has a unique solution in $\mathcal{V}$ with $u_{|\partial D} = g$, by the Lax-Milgram lemma. In the continuous setting, problem (3) yields $(u_D)_{|\Omega} = u_\Omega$ and $(u_D)_{|\omega} = u_\omega$ but when we discretize (3), the situation is rather different.

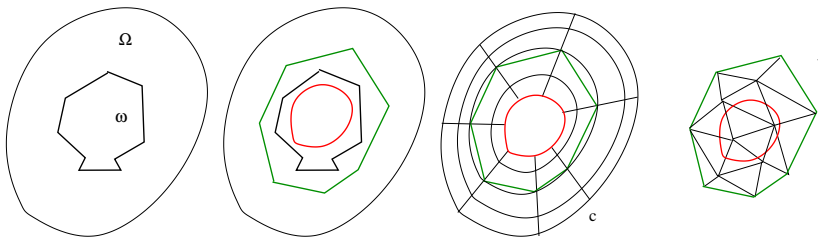

Figure 1 The domain $D = \Omega \cup \omega$ with $\Omega \cap \omega = \emptyset$ (left-side). The domain $D = \Omega_H \cup \omega_h$ with $\Omega_H \cap \omega_h \neq \emptyset$. In particular, $\gamma = \partial\omega_h$ is the green polygonal and $\Gamma = \partial\Omega_H \setminus \partial D$ is the red line (center-left). An example of mesh with curved quadrilaterals in Ω_H (center-right) and with straight triangles in ω_h (right-side).

We wish to introduce different types of meshes τ_H and τ_h in two sub-domains Ω_H, ω_h, of D, with $\Omega_H \cup \omega_h = D$ (as in Fig. 1, center-left). Let τ_H be a mesh of curved quadrangles over Ω_H with $\Omega \subset \Omega_H$, and τ_h a mesh of straight triangles over ω_h with $\omega \subset \omega_h$. The two meshes τ_H, τ_h are shape regular and quasi-uniform, with maximal diameters H, h, respectively. In the general case, we have $\Omega_H \cap \omega_h \neq \emptyset$ and we denote by Γ the smooth curve $\partial\Omega_H \cap \mathring{\omega}_h$ (the red line in Fig. 1) and we keep on denoting by γ the polygonal curve $\partial\omega_h \cap \mathring{\Omega}_H$ (the green polygonal in Fig. 1). These overlapping triangulations can be completely independent to each other. Hence, a priori, they do not match on $\Omega_H \cap \omega_h$ and, neither the edges of τ_H on the curve γ coincide with edges of τ_h, nor the edges of τ_h on the curve Γ coincide with edges of τ_H (as in Fig. 1, right-center and right-side).

3 | INTERPOLATION SPACES : TWO FINITE ELEMENTS OF CLASS $\mathcal{C}^1$

We use the reduced or minimal Hsieh-Clough-Tocher (rHCT) finite element space on τ_h (see[10]) and Hermite-Bézier (HB) finite elements on τ_H (see[11]) within a isoparametric approach.

3.1 | The space of reduced Hsieh-Clough-Tocher finite elements

Locally, the rHCT finite element is the triple $(T, \mathcal{P}_{loc}(T), \Sigma(T))$ where T denotes a triangle of the mesh τ_h, $\mathcal{P}_{loc}(T)$ the local space of functions defined on that triangle and $\Sigma(T)$ a set of unisolvent dofs for the functions in the local space (see[11]). The indices i, $i+1$, $i+2$, in Definition 1 below, take values $1, 2, 3$. When $i+1 > 3$ (resp. $i+2 > 3$), we replace it by $[(i+1) \mod 3] + 1$ (resp. $[(i+2) \mod 3] + 1$).

Definition 1. Let $T = [V_1, V_2, V_3]$ be the triangle of vertices V_1, V_2, V_3. The triangle T is divided into three sub-triangles $\mathtt{B}_i = [G, V_{i+1}, V_{i+2}]$ where G is the barycenter of T (see Figure 2). The rHCT finite element associated with T is the triple $(T, \mathcal{P}_{loc}(T), \Sigma(T))$, where $\mathcal{P}_{loc}(T)$ is the polynomial space of functions $w \in C^1(T)$ such that $w_{|\mathtt{B}_i} \in \mathbb{P}_3(\mathtt{B}_i)$ and $(\partial_n w)_{|\mathtt{b}_i} \in \mathbb{P}_1(\mathtt{b}_i)$ for any edge $\mathtt{b}_i \in \partial\mathtt{B}_i \cap \partial T$. Here above,

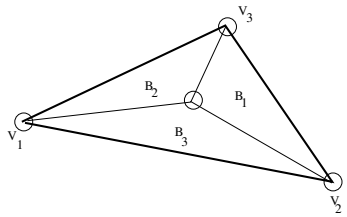

Figure 2 Any triangle $T = [V_1, V_2, V_3]$ of the mesh τ_h is cut into three triangles $\mathtt{B}_i$: each $\mathtt{B}_i = [G, V_m, V_\ell]$ having vertices in V_m, V_ℓ with $m, \ell \in \{1, 2, 3\} \setminus \{i\}$ and at the barycenter G (denoted by the small circle at the interior) of the triangle T. We can thus reconstruct the height $u_h(V_i)$ of the function u_h at the three vertices V_i of T and the tangent plane to the surface u_h at the vertices V_i, as generated by $\partial_x u_h(V_i), \partial_y u_h(V_i)$.

n is the outward normal vector to ∂T, $\mathtt{b}_i$ the edge on ∂T that does not insist in the vertex V_i and $(\partial_n w)_{|\mathtt{b}_i}$ the normal derivative of w at $\mathtt{b}_i$, and $\Sigma(T)$ is the set defined by the following functionals:

$$(j=0) \qquad w \mapsto w(V_i)\,, \qquad (j=1) \qquad w \mapsto (\mathbf{grad}\, w)(V_i) \cdot (V_{i+1} - V_i)\,, \qquad (j=2) \qquad w \mapsto (\mathbf{grad}\, w)(V_i) \cdot (V_{i+2} - V_i),$$

where $(\mathbf{grad} w)(V_i) \cdot (V_{i+1} - V_i)$ is the directional derivative of w on $[V_i, V_{i+1}]$ and j denotes the degree of freedom type. Note that $(\mathbf{grad}\, w)(V_i) \cdot (V_{i+1} - V_i) = (\partial_n w)_{|\mathtt{b}_{i+1}}(V_i) - (\partial_n w)_{|\mathtt{b}_i}(V_i)$.

We thus have on the polygonal domain ω_h the discrete space

$$\mathcal{V}_h = \{v \in C^1(\omega_h),\, v_{|T} \in \mathcal{P}_{loc}(T),\, \forall\, T \in \tau_h\,\},$$

with $\mathcal{P}_{loc}(T)$ given in Definition 1. We denote by $\{\phi_i\}_{i=1,3N_h}$ the basis of $\mathcal{V}_h$ in duality with the dofs of Definition 1 associated with the N_h nodes of τ_h and we refer to[12] for its detailed construction. See[13] for application of these FEs in the context of plasma equilibrium simulations.

3.2 | The space of isoparametric Hermite-Bézier finite elements

Let be τ_H a mesh of curved quadrangles over Ω_H where we consider isoparametric bi-cubic Hermite-Bézier (HB) finite elements[11], in the physical space, following the idea described in[4]. We go into the details of this delicate construction: (i) we start with the approximation of a curve, (ii) then of a domain, (iii) and finally of a field w on that domain. This approach generalizes the one proposed in[14] on Cartesian meshes in the context of plasma equilibrium simulations. For any $S \subset \mathbb{R}^d$, $d = 1, 2$, we denote by $\mathcal{Q}_3(S)$, the space of bi-cubic polynomials on S, namely polynomials defined in S, of degree at most 3 with respect to each of the d real variables. Note that $\mathcal{Q}_3(S) = \mathbb{P}_3(S)$ for $d = 1$.

3.2.1 | In one parametric dimension

We start by defining the HB FE on the reference interval $\hat{e} = [0, 1]$ and by presenting the construction of Γ_H, a $\mathcal{C}^1$ approximation of a curve $\Gamma \subset \mathbb{R}^2$ by these FEs.

Definition 2. The Hermite-Bézier finite element on $\hat{e} = [0,1]$ is the triple $(\hat{e}, P_{loc}(\hat{e}), \Sigma(\hat{e}))$ where $P_{loc}(\hat{e}) = \mathcal{Q}_3(\hat{e})$ and $\Sigma(\hat{e})$ is the set of functionals

$$(j=0) \qquad v \mapsto v(\diamond), \qquad v \mapsto \partial_s v(\diamond) \qquad (j=1)$$

acting on $v \in P_{loc}(\hat{e})$. Here, $s \in \hat{e}$ is the polynomial variable, j denotes the degree of freedom type and $(\diamond)$ varies between the two vertices $(0), (1)$ of $\hat{e}$.

In Definition 2, the space $P_{loc}(\hat{e}) = \mathbb{P}_3(\hat{e})$ and $\operatorname{card}\Sigma(\hat{e}) = 4$. It is well-known that we can set $P_{loc}(\hat{e}) = \operatorname{span}\{H_i^j(s),\, j=0,1,\, i=1,2\}$ being H_i^ℓ the cubic polynomials defined on $\hat{e}$ as

$$H_1^0(s) = (1+2\,s)\,(1-s)^2, \qquad H_1^1(s) = s\,(1-s)^2,$$

$$H_2^0(s) = (3-2\,s)\,s^2 \;(= H_1^0(1-s)), \qquad H_2^1(s) = (1-s)\,s^2 \;(= H_1^1(1-s)).$$

These polynomials H_i^j verify

$$H_1^0(0) = 1,\ (H_1^0)'(0) = 0,\ H_1^0(1) = 0,\ (H_1^0)'(1) = 0,$$

$$H_1^1(0) = 0,\ (H_1^1)'(0) = 1,\ H_1^1(1) = 0,\ (H_1^1)'(1) = 0,$$

$$H_2^0(0) = 0,\ (H_2^0)'(0) = 0,\ H_2^0(1) = 1,\ (H_2^0)'(1) = 0,$$

$$H_2^1(0) = 0,\ (H_2^1)'(0) = 0,\ H_2^1(1) = 0,\ (H_2^1)'(1) = 1\,.$$

Suppose that we have a parametric representation of Γ as

$$\Gamma = \left\{ \mathbf{X} = \begin{pmatrix} x \\ y \end{pmatrix},\, x = t,\, y = y(t),\, t \in [a,b] \right\},$$

with t acting as global parameter. Note that Γ is the graph of the function $y = y(x)$ for $x \in [a,b]$. The curve Γ is regular if $\mathbf{X}$ is component-wise $\mathcal{C}^1([a,b])$. The tangent vector to Γ at a point $\mathbf{X}(t)$ is $\frac{d\mathbf{X}}{dt}(t) = (1, y'(t))^\top$. The curve Γ is thus regular if $\frac{d\mathbf{X}}{dt}$ is component-wise $\mathcal{C}^0(]a,b[)$. For a regular curve Γ, the arc-length parameter along the curve is the function

$$\xi(t) = \int_a^t \|\frac{d\mathbf{X}}{dt}(\sigma)\|\, d\sigma, \qquad \text{with} \quad \|\frac{d\mathbf{X}}{dt}(.)\| = \sqrt{1 + (y'(.))^2}.$$

We have that ξ is $\mathcal{C}^1([a,b])$ and $\xi'(t) = \|\frac{d\mathbf{X}}{dt}(t)\| > 0$, thus $\xi : [a,b] \to [0, l(\Gamma)]$ is a diffeomorphism, with $\xi(b) = l(\Gamma)$ the length of Γ. If $t(\xi)$ is the inverse of $\xi(t)$, we have that the same curve Γ can be defined equivalently as

$$\Gamma = \left\{ \mathbf{X} = \begin{pmatrix} \xi \\ p(\xi) \end{pmatrix},\, p(\xi) = y(t(\xi)),\, \xi \in [0, l(\Gamma)\,] \right\}$$

and it holds

$$\frac{d\mathbf{X}}{d\xi} = \frac{d\mathbf{X}}{dt}\,\frac{dt}{d\xi}\,.$$

When we represent $\mathbf{X}(\xi)$ by a piece-wise combination $\mathbf{X}_H(\xi)$ of Hermite-Bézier polynomials, to obtain a $\mathcal{C}^1$ curve Γ_H, we have to adjust the coefficients of this combination in order to restore the continuity of the arc-length derivative $\frac{d\mathbf{X}_H}{d\xi}$ at the points on Γ_H shared by adjacent curved segments.

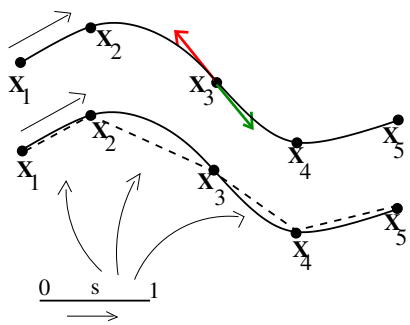

Figure 3 The oriented curve Γ (solid line) is divided into 4 curved segments e. The internal point $\mathbf{X}_3$ is the extremity of two adjacent segments, e^- (resp., e^+) insisting in $\mathbf{X}_3$ from the left (resp., right), according to the orientation of Γ. The tangent vector at $\mathbf{X}_3 \in \Gamma_H$ has to be continuous thus the red and green vectors have to belong to the same straight line (tangent to Γ at $\mathbf{X}_3$) and to be of the same length. The polygonal (dashed line) has straight sides with extremities $\xi(\zeta_k^e)$, where $\zeta^e : [0,1] \to e$ (bottom arrows) associated with $e = [t_k, t_{k+1}]$, for each value of $k = 1, ..., 4$.

Let us consider a uniform grid of $N+1$ points $\mathbf{X}_k \in \Gamma$, $k = 1, ..., N+1$ (see Fig. 3 for an example with 5 points). We can write either $\mathbf{X}_k = (t_k, y(t_k))$, with $t_k = a + k\,\delta t$ and $\delta t = (b-a)/N$ or, equivalently, $\mathbf{X}_k = (\xi_k, g(\xi_k))$, with $\xi_k = \xi(t_k)$. Then, by introducing the variable $\zeta^e(s) = s\,t_{k+1} + (1-s)\,t_k$, with $s \in [0,1]$, any point $\mathbf{X}$ belonging to the curved interval $e \subset \Gamma$, of extremities $\mathbf{X}_k$ and $\mathbf{X}_{k+1}$, can be written with

$$\widehat{\mathbf{X}}(s) := \mathbf{X}(\xi) = \mathbf{X}(\xi(\zeta^e(s))), \qquad \frac{d\,\widehat{\mathbf{X}}}{d\,s} := \frac{d\,\mathbf{X}}{d\,\xi}\,\frac{d\,\xi}{d\,\zeta^e}\,\frac{d\,\zeta^e}{d\,s},$$

and

$$\xi(\zeta^e(s)) = \xi_k + \int_{t_k}^{t(s)} \|\frac{d\,\mathbf{X}}{d\,t}(\zeta^e)\|\,d\zeta^e = \xi_k + \int_0^1 \|\frac{d\,\mathbf{X}}{d\,t}(\zeta^e(s))\|\,\frac{d\,\zeta^e}{d\,s}\,d\,s\,.$$

We wish to represent Γ by a curve $\Gamma_H = \cup_{k=1}^N e_k$ with

$$e_k = \left\{ \mathbf{X}_{H_{|e_k}} = \begin{pmatrix} \xi \\ p_H(\xi) \end{pmatrix}, \xi = \xi(t),\, t \in [t_k, t_{k+1}\,] \right\},$$

with $p_H(\xi) \approx p(\xi)$. To have Γ_H reconstructed by HB cubic polynomials means that, for each e_k,

$$\xi \in [\xi_k, \xi_{k+1}\,], \qquad (\mathbf{X}_H(\xi))_{|e_k} = \widehat{\mathbf{X}}(s) = \sum_{i=1}^{2}\sum_{j=0}^{1} \mathbf{X}_i^{j,e}\,\beta_i^{j,e} H_i^j(s), \qquad s \in [0,1].$$

In order to ensure that the reconstructed curve Γ_H is $\mathcal{C}^1$, the coefficients $\mathbf{X}_i^{j,e}\,\beta_i^{j,e}$ have to be such that $\frac{d\,\mathbf{X}_H}{d\,\xi}$ is continuous passing from one curved edge to the adjacent one. High-order continuity in the physical space is achieved if the arc-length derivative is continuous at

the internal grid points ξ_k, namely

$$\frac{d\,\widehat{\mathbf{X}}}{d\,s}(0) = +\left(\frac{d\xi}{d\zeta}\frac{d\zeta^e}{ds}\right)\frac{d\mathbf{X}_H}{d\xi}(\xi_k), \qquad \frac{d\,\widehat{\mathbf{X}}}{d\,s}(1) = -\left(\frac{d\xi}{d\zeta}\frac{d\zeta^e}{ds}\right)\frac{d\mathbf{X}_H}{d\xi}(\xi_k).$$

Therefore,

$$\begin{aligned}
\mathbf{X}_1^{0,e} &= \mathbf{X}_k, & \beta_1^{0,e} &= 1,\\
\mathbf{X}_1^{1,e} &= \left(\frac{d\mathbf{X}}{d\,\xi}\right)(\xi_k), & \beta_1^{1,e} &= +\left(\frac{d\xi}{d\zeta}\frac{d\zeta^e}{ds}\right)(0)\\
\mathbf{X}_2^{0,e} &= \mathbf{X}_{k+1}, & \beta_2^{0,e} &= 1,\\
\mathbf{X}_2^{1,e} &= \left(\frac{d\mathbf{X}}{d\,\xi}\right)(\xi_{k+1}), & \beta_2^{1,e} &= -\left(\frac{d\xi}{d\zeta}\frac{d\zeta^e}{ds}\right)(1).
\end{aligned}$$

If Γ is not known analytically but provided by a finite set of points $\mathbf{X}_k$, we replace derivatives by suitable finite difference schemes.

3.2.2 | In two parametric dimensions

Let us define the HB FE on the reference square $\hat{Q} = [0,1]^2$ and go through the steps of the construction, by these FEs, of a $\mathcal{C}^1$ representation Ω_H of a domain $\Omega \subset \mathbb{R}^2$, with $\overset{\circ}{\Omega} \neq \emptyset$.

Definition 3. The Hermite-Bézier finite element on $\hat{Q} = [0,1]^2$ is the triple $(\hat{Q}, P_{loc}(\hat{Q}), \Sigma(\hat{Q}))$ where $P_{loc}(\hat{Q}) = \text{span}\,\{H_i^j(s,t),\ i = 1,...,4,\ j = 0,...,3\}$ and $\Sigma(\hat{Q})$ is the set defined by functionals

$$(j=0) \qquad v \mapsto v(\diamond,\diamond), \qquad v \mapsto \partial_s v(\diamond,\diamond) \qquad (j=1)$$

$$(j=2) \qquad v \mapsto \partial_t v(\diamond,\diamond) \qquad v \mapsto \partial_{st}^2 v(\diamond,\diamond) \qquad (j=3)$$

with j denoting the degree of freedom type and $(\diamond,\diamond)$ varying among the four vertices $(0,0),(1,0),(0,1),(1,1)$ of $\hat{Q}$.

In Definition 3, the space $P_{loc}(\hat{Q}) = \mathbb{Q}_3(\hat{Q})$ and $\text{card}\,\Sigma(\hat{Q}) = 16$. It is well-known that we can set $P_{loc}(\hat{Q}) = \text{span}\,\{H_i^j(s,t),\ j = 0,...,3,\ i = 1,...,4\}$ being H_i^j the bi-cubic Hermite-Bézier basis function associated with the ith vertex of $\hat{Q}$ for the jth degree of freedom stated in Definition 3. For $i = 1$ we have for example

$$\begin{aligned}
H_1^0(s,t) &= H_1^0(s)\,H_1^0(t), \quad H_1^1(s,t) = H_1^1(s)\,H_1^0(t),\\
H_1^2(s,t) &= H_1^0(s)\,H_1^1(t), \qquad H_1^3(s,t) = H_1^1(s)\,H_1^1(t).
\end{aligned} \tag{4}$$

The basis functions for the vertices $i = 2,3,4$ can be defined as

$$H_2^j(s,t) = H_1^j(1-s,t), \quad H_3^j(s,t) = H_1^j(1-s,1-t), \quad H_4^j(s,t) = H_1^j(s,1-t),$$

for any $j = 0,...,3$.

Let us suppose to be given with a parametric representation of Ω as

$$\Omega = \left\{ \mathbf{X} = \begin{pmatrix} x \\ y \end{pmatrix},\ x = x(z,w),\ y = y(z,w),\ z \in [a_z,b_z],\ w \in [a_w,b_w] \right\}$$

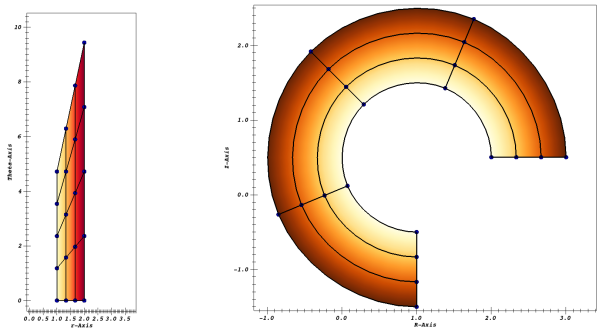

Figure 4 Annular mesh in the parametric (left) and in the physical (right) spaces. Color scaling in both cases is set on the small radius (r) of each layer.

with z, w acting as global parameters. The domain Ω is regular if $\mathbf{X}$ is component-wise $\mathcal{C}^1(K)$, with $K = [a_z, b_z] \times [a_w, b_w]$. The tangent plane to Ω at a point $\mathbf{X}^*$ is generated by the two vectors

$$\partial_z \mathbf{X}(z^*, w^*) = \begin{pmatrix} \partial_z x(z^*, w^*) \\ \\ \partial_z y(z^*, w^*) \end{pmatrix}, \qquad \partial_w \mathbf{X}(z^*, w^*) = \begin{pmatrix} \partial_w x(z^*, w^*) \\ \\ \partial_w y(z^*, w^*) \end{pmatrix},$$

which are assumed to be linearly independent, namely, $\det J(z^*, w^*) \neq 0$ with $J(.,.)$ the 2×2 Jacobian matrix $(\partial_z \mathbf{X}(.,.)\,, \partial_w \mathbf{X}(.,.))$. We assume that Ω is an oriented surface and that it exists a diffeomorphism $\pi : K \to C$ with $C = [0, L_z] \times [0, L_w]$, $L_z, L_w \in \mathbb{R}^+$, and $(\xi_z, \xi_w) := \pi(z, w)$, such that "the diagram commutes", namely $(x(z,w), y(z,w)) = (\,X(\pi(z,w)), Y(\pi(z,w))\,)$. The domain Ω can be equivalently defined as

$$\Omega = \left\{ \mathbf{X} = \begin{pmatrix} X(\xi_z, \xi_w) \\ \\ Y(\xi_z, \xi_w) \end{pmatrix}, \xi_z \in [0, L_z],\, \xi_w \in [0, L_w] \right\}.$$

We keep on considering (ξ_z, ξ_w) as arc-length like coordinates.

Let us consider a uniform grid of $N_p = (N_x + 1) \times (N_y + 1)$ points $\mathbf{X}_k \in \Omega$, $k = 1, ..., N_p$ We can write $\mathbf{X}_k = (x_k, y_k)$ with

$$x_k = x(z_i, w_j), \quad y_k = y(z_i, w_j), \qquad k = (j-1)\,N_x + i,$$

$$z_i = a_z + i\,\delta z, \quad w_j = a_w + j\,\delta w, \quad i = 1, ..., N_x,$$

$$\delta z = \tfrac{(b_z - a_z)}{N_x}, \quad \delta w = \tfrac{(b_w - a_w)}{N_y}, \quad j = 1, ..., N_y.$$

We wish to represent Ω by a surface $\Omega_H = \cup_{e=1}^{N_{el}} Q_e$ with $N_{el} = N_x \times N_y$ curved elements

$$Q_e = \left\{ \mathbf{X}_H = \begin{pmatrix} X_H(\xi_z, \xi_w) \\ \\ Y_H(\xi_z, \xi_w) \end{pmatrix}, (\xi_z, \xi_w) \in C_e = \pi(K_e) \right\}$$

with K_e domain for (z, w) to have $\mathbf{X}_H \in Q_e$, and $X_H(.,.) \approx X(.,.)$, $Y_H(.,.) \approx Y(.,.)$. From now on, we work with arc-length like variables ξ_z and ξ_w for which we change the notation into ξ_s and ξ_t, respectively, as we are going to link the global construction of Ω_H to HB

functions H_i^j locally defined on $[0,1]^2$ in terms of s and t. To have Ω_H piece-wisely reconstructed by HB cubic polynomials means that, for each Q_e,

$$(\xi_z, \xi_w) \in C_e, \qquad \mathbf{X}_H(\xi_z, \xi_w) = \widehat{\mathbf{X}}(s,t) = \sum_{i=1}^{4}\sum_{j=0}^{3} \mathbf{X}_i^{j,e}\, \beta_i^{j,e} H_i^j(s,t). \tag{5}$$

To describe curved domain, we need to consider three levels of variables : the reference space (s,t), the parametric space (ζ_s, ζ_t) and the arc-length space (ξ_s, ξ_t). In the physical space, the element Q_e has curved edges in the variables ξ_s and ξ_t. In the parametric space (ζ_s, ζ_t), curved lines become straight and Q_e looks like a quadrilateral (see Fig. 4). For the application we will consider here, we suppose that variables ξ_s and ξ_t act separately, that is the mapping between the (ξ_s, ξ_t) and (s,t) coordinate systems reads

$$\mathbf{X}(\xi_s, \xi_t) = \mathbf{X}(\xi_s(\zeta_s(s)), \xi_t(\zeta_t(t)) = \widehat{\mathbf{X}}(s,t) \tag{6}$$

with the functions (ζ_s, ζ_t) suitably defined as follows. Let Q_e be a curved element with vertices $\mathbf{X}_{g(i)}$, being $g(i)$ the global number of the ith local vertex, $i = 1, ..., 4$, then its curved sides $\mathcal{S}_i$ are

$$\begin{aligned}
\mathcal{S}_1 &= \{\mathbf{X}(\xi_s(\zeta_s(s)), \xi_t(\zeta_t(0))) = \widehat{\mathbf{X}}(s,0)\}, \quad \mathbf{X}_{g(1)} \to \mathbf{X}_{g(2)},\\
\mathcal{S}_2 &= \{\mathbf{X}(\xi_s(\zeta_s(1)), \xi_t(\zeta_t(t))) = \widehat{\mathbf{X}}(1,t)\}, \quad \mathbf{X}_{g(2)} \to \mathbf{X}_{g(3)},\\
\mathcal{S}_3 &= \{\mathbf{X}(\xi_s(\zeta_s(s)), \xi_t(\zeta_t(1))) = \widehat{\mathbf{X}}(s,1)\}, \quad \mathbf{X}_{g(4)} \to \mathbf{X}_{g(3)},\\
\mathcal{S}_4 &= \{\mathbf{X}(\xi_s(\zeta_s(0)), \xi_t(\zeta_t(t))) = \widehat{\mathbf{X}}(0,t)\}, \quad \mathbf{X}_{g(1)} \to \mathbf{X}_{g(4)},
\end{aligned}$$

with $s, t \in [0,1]$ and, respectively,

$$\zeta_s(s) = s\, z_{i+1} + (1-s)\, z_i, \qquad \zeta_t(t) = t\, w_{j+1} + (1-t)\, w_j.$$

Examples 1 and 2 illustrate the three levels of variables. Note that the mapping between s, t and ζ_s, ζ_t is linear and that between ζ_s, ζ_t and ξ_s, ξ_t is cubic. By the chain rule, we obtain:

$$\frac{\partial \widehat{\mathbf{X}}}{\partial s} = \frac{d\xi_s}{d\zeta_s}\frac{d\zeta_s}{ds}\frac{\partial \mathbf{X}}{\partial \xi_s}, \qquad \frac{\partial \widehat{\mathbf{X}}}{\partial t} = \frac{d\xi_t}{d\zeta_t}\frac{d\zeta_t}{dt}\frac{\partial \mathbf{X}}{\partial \xi_t}, \qquad \frac{\partial^2 \widehat{\mathbf{X}}}{\partial s \partial t} = \frac{d\xi_s}{d\zeta_s}\frac{d\zeta_s}{ds}\frac{d\xi_t}{d\zeta_t}\frac{d\zeta_t}{dt}\frac{\partial^2 \mathbf{X}}{\partial \xi_s \partial \xi_t}.$$

The $\beta_i^{j,e}$ are specific scale factors that arrange the $\mathcal{C}^1$ inter-element continuity and the $\mathbf{X}_i^{j,e}$ are specific functions of the physical coordinates at the element vertices $g(i)$. Since metric tensor and Jacobian differ between elements, each element Q_e has specific coefficients $\beta_i^{j,e}$, for each node i and degree of freedom j to guarantee the $\mathcal{C}^1$ inter-element continuity. We want to enforce continuity in the physical space[4]. Therefore, we need to share the derivatives along arc length coordinates ξ_s and ξ_t, the integrated curves length in the physical space,

respectively associated with the parameters coordinates s and t. The coefficients and the scale factors in the equation (5) are:

$$\mathbf{X}_i^{0,e} = \mathbf{X}_{g(i)} \qquad \beta_i^{0,e} = 1$$

$$\mathbf{X}_i^{1,e} = \left(\frac{\partial \mathbf{X}}{\partial \xi_s}\right)_{g(i)} \qquad \beta_i^{1,e} = \pm\left(\frac{d\xi_s}{d\zeta_s}\frac{d\zeta_s^e}{ds}\right)_{g(i)}$$

$$\mathbf{X}_i^{2,e} = \left(\frac{\partial \mathbf{X}}{\partial \xi_t}\right)_{g(i)} \qquad \beta_i^{2,e} = \pm\left(\frac{d\xi_t}{d\zeta_t}\frac{d\zeta_t^e}{dt}\right)_{g(i)}$$

$$\mathbf{X}_i^{3,e} = \left(\frac{\partial^2 \mathbf{X}}{\partial \xi_s \partial \xi_t}\right)_{g(i)} \qquad \beta_i^{3,e} = \beta_i^{1,e}\beta_i^{2,e}.$$

The $\mathbf{X}_i^{j,e}$ are related to the bi-cubic Hermite coefficients in the arc-physical space and are shared at each node $g(i)$ while the scale factors $\beta_i^{j,e}$ are different in each element e that shares the node $g(i)$. The sign of $\beta_i^{2,e}$ and $\beta_i^{3,e}$ is plus or minus, depending on the vertex position in Q_e (see Fig. 5). The scale factors generalizes the bi-cubic Hermite FEs without compromising the accuracy and allowing the implementation of the adaptive mesh refinement [4].

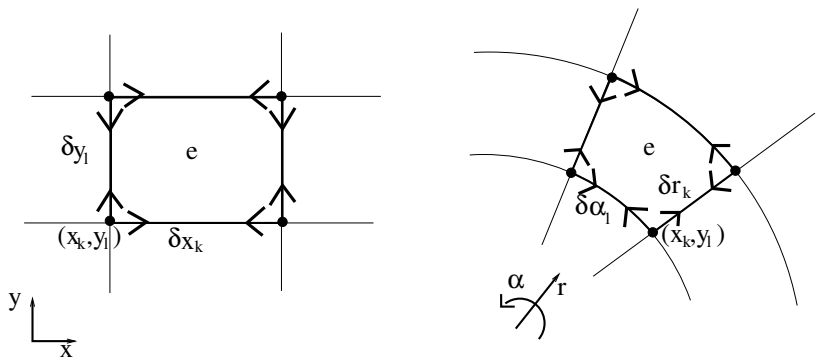

Figure 5 A cell e for a quadrangular mesh with straight edges (left) or curved edges (right).

Example 1. Let us consider a square domain

$$\Omega_H = \left\{ \mathbf{X} = \begin{pmatrix} x \\ y \end{pmatrix}, x^0 \le x \le x^\star,\ y^0 \le y \le y^\star \right\}$$

where ^{0} and * stand respectively for minimal and maximal values. Let us consider a mesh of straight rectangles over Ω_H. Then

$$\xi_s = x, \quad \xi_t = y, \quad \zeta_s = x, \quad \zeta_t = y, \quad \zeta_s^e = x_k + s\delta x_k, \quad \zeta_t^e = y_l + t\delta y_l$$

where $Q_e = [x_k, x_k + \delta x_k] \times [y_\ell, y_\ell + \delta y_\ell]$ is the rectangle with the left bottom corner in (x_k, y_ℓ) and sizes δx_k, δy_ℓ, in the x, y directions, respectively. We thus have

$$\frac{\partial \mathbf{X}}{\partial \xi_s} = \begin{pmatrix} 1 \\ 0 \end{pmatrix}, \quad \frac{\partial \mathbf{X}}{\partial \xi_t} = \begin{pmatrix} 0 \\ 1 \end{pmatrix}, \quad \frac{\partial^2 \mathbf{X}}{\partial \xi_s \partial \xi_t} = \begin{pmatrix} 0 \\ 0 \end{pmatrix}$$

and the scales have a sign which depends on the vertex position in Q_e (see Fig. 5):

$$\beta^{1,e}_{k,l} = \delta x_k, \quad \beta^{1,e}_{k+1,l} = -\delta x_k, \quad \beta^{2,e}_{k,l} = \delta y_l \quad \beta^{2,e}_{k,l+1} = -\delta y_l \,.$$

Example 2. Let us consider an annular domain

$$\Omega_H = \left\{ \mathbf{X} = \mathbf{X}_0 + \begin{pmatrix} r\cos\alpha \\ \\ r\sin\alpha \end{pmatrix}, r^0 \le r \le r^\star, \alpha^0 \le \alpha \le \alpha^\star \right\}$$

where ^{0} and * stand respectively for minimal and maximal values. Then,

$$\xi_s = r, \quad \xi_t = r\alpha, \quad \zeta_s = r, \quad \zeta_t = \alpha, \quad \zeta^e_s = r_k + s\delta r_k, \quad \zeta^e_t = \alpha_l + t\delta\alpha_l$$

$$\frac{\partial \mathbf{X}}{\partial \xi_s} = \begin{pmatrix} \cos\alpha \\ \\ \sin\alpha \end{pmatrix}, \quad \frac{\partial \mathbf{X}}{\partial \xi_t} = \begin{pmatrix} -\sin\alpha \\ \\ \cos\alpha \end{pmatrix}, \quad \frac{\partial^2 \mathbf{X}}{\partial \xi_s \partial \xi_t} = \frac{1}{r}\begin{pmatrix} -\sin\alpha \\ \\ \cos\alpha \end{pmatrix}$$

The scales have a sign which depends on the vertex position (see Fig. 5):

$$\beta^{1,e}_{k,l} = \delta r_k, \quad \beta^{1,e}_{k+1,l} = -\delta r_k, \quad \beta^{2,e}_{k,l} = r_k\delta\alpha_l \quad \beta^{2,e}_{k,l+1} = -r_k\delta\alpha_l \,.$$

3.2.3 | Field interpolation

For any given quadrangular element Q_e of the mesh τ_H, a physical variable, such as the scalar field w, is expanded in the $\mathcal{C}^1$ continuous basis as follows

$$w(x,y) = \hat{w}(s,t) = \sum_{i=1}^{4}\sum_{j=0}^{3} w^j_{g(i)}\, \beta^{e,j}_i\, H^j_i(s,t)\,, \quad F_e(s,t) = (x,y) \in Q_e. \tag{7}$$

The coefficients $w^j_{g(i)}$ are the dofs of w at node $\mathbf{X}_g(i)$ shared by all elements Q_e insisting into $\mathbf{X}_{g(i)}$. These dofs are the value, the s-derivative, the t-derivative, and the s,t cross-derivative of the physical scalar field w at the location of the grid node. The scale factors are a geometric grid property and therefore time independent and identical for each physical quantity. We thus consider the discrete space

$$\mathcal{V}_H = \{z \in C^1(\Omega_H),\, z_{|Q_e} \circ F_e^{-1} \in \mathcal{P}_{loc}(\hat{Q}),\, \forall\, Q_e \in \tau_H\}$$

with $\mathcal{P}_{loc}(\hat{Q})$ defined in Definition 3. We denote by $\{\psi_k\}_{k=1,4N_h}$ the basis of $\mathcal{V}_H$ in duality with the dofs of Definition 3 associated with vertices $V_i \in \tau_H$.

3.3 | From local to global coordinates and return

On the rHCT side, we have the value, the x-derivative and the y-derivative of the field u_h in the physical space whereas, on the HB side, we have the value, the s-derivative, the t-derivative, and the s,t cross-derivative of the field u_H expressed in the local variables. We go back and forth from reference to physical coordinates as follows. For the values, we know that for a point (x,y), if we think to u^G (resp.,

u^L) as the discrete field, either u_H or u_h, in the physical global (resp., reference local) variables, then

$$u^G(x,y) = u^L(s,t)\,\eta^1(s,t) \qquad \text{if} \qquad (x,y) = \mathbf{x}(s,t)\,, \tag{8}$$

where $\eta^1(s,t)$ is the scalar length unit change at the point (s,t). But for derivatives, the rule is different, more precisely let us introduce $J_h(s,t)^\top$, the transpose of the 2×2 Jacobian matrix $J(s,t)$ for the mapping defined in (5), that is

$$J(s,t) = \begin{pmatrix} \partial_s\, x(s,t) & \partial_t\, x(s,t) \\ \partial_s\, y(s,t) & \partial_t\, y(s,t) \end{pmatrix} = (\,\boldsymbol{\eta}^2(s,t)\,,\,\boldsymbol{\eta}^3(s,t)\,).$$

Lemma 1. The first order derivatives of u^L with respect to the local variables s, t, evaluated at (s,t), are given by

$$\partial_s\, u^L(s,t) = \nabla_{x,y} u^G(x,y)\cdot \boldsymbol{\eta}^2(s,t), \qquad \partial_t\, u^L(s,t) = \nabla_{x,y} u^G(x,y)\cdot \boldsymbol{\eta}^3(s,t), \tag{9}$$

where the vector $\boldsymbol{\eta}^2(s,t)$ stands for $(\partial_s x,\, \partial_s y)^\top$, the vector $\boldsymbol{\eta}^3(s,t)$ stands for $(\partial_t y,\, \partial_t y)^\top$, both evaluated at the point (s,t), and $\nabla_{x,y} u^G(x,y)$ is the gradient vector of u^G with respect to the global physical variables x, y, evaluated at (x,y).

Proof. We have for example

$$\partial_s\, u^L(s,t) = \partial_x\, u^G(x,y)\,\partial_s\, x(s,t) + \partial_y\, u^G(x,y)\,\partial_s\, y(s,t)$$

and similarly

$$\partial_t\, u^L(s,t) = \partial_x\, u^G(x,y)\,\partial_t\, x(s,t) + \partial_y\, u^G(x,y)\,\partial_t\, y(s,t).$$

thus the result, by relying on the expression of $\boldsymbol{\eta}^2(s,t)$ and $\boldsymbol{\eta}^3(s,t)$. □

Lemma 1 yields $\nabla_{s,t}\, u^L(s,t) = J(s,t)^\top\, \nabla_{x,y}\, u^G(x,y)$ and conversely

$$\nabla_{x,y}\, u^G(x,y) = (J(s,t)^\top)^{-1}\, \nabla_{s,t}\, u^L(s,t). \tag{10}$$

We rely on a classical formalism to write the second cross-derivatives of the discrete function u_H or u_h. The first notation involves two matrices $A, B \in \mathbb{R}^{2\times 2}$ to give the scalar quantity $A : B \in \mathbb{R}$ as follows

$$A = (A_{i,j}),\, B = (B_{i,j}), \qquad A : B = \sum_{i,j} A_{i,j}\, B_{i,j}$$

and the second, two vectors $\mathbf{v}, \mathbf{w} \in \mathbb{R}^2$ to define the matrix $\mathbf{v}\otimes\mathbf{w} \in \mathbb{R}^{2\times 2}$ with

$$\mathbf{v} = (v_i),\, \mathbf{w} = (w_j), \qquad (\mathbf{v}\otimes\mathbf{w})_{i,j} = v_i\, w_j\,.$$

Lemma 2. The second order derivatives of u^L with respect to the local variables s, t, evaluated at (s,t), are given by

$$\partial^2_{st} u^L(s,t) = \boldsymbol{\eta}^4(s,t) \cdot \nabla_{x,y} u^G(x,y) + \boldsymbol{\eta}^2(s,t) \otimes \boldsymbol{\eta}^3(s,t) : Hess_{x,y} u^G(x,y),$$

$$\partial^2_{ss} u^L(s,t) = \boldsymbol{\eta}^5(s,t) \cdot \nabla_{x,y} u^G(x,y) + \boldsymbol{\eta}^2(s,t) \otimes \boldsymbol{\eta}^2(s,t) : Hess_{x,y} u^G(x,y),$$

$$\partial^2_{tt} u^L(s,t) = \boldsymbol{\eta}^6(s,t) \cdot \nabla_{x,y} u^G(x,y) + \boldsymbol{\eta}^3(s,t) \otimes \boldsymbol{\eta}^3(s,t) : Hess_{x,y} u^G(x,y),$$

where the vector $\boldsymbol{\eta}^4(s,t)$ (resp., $\boldsymbol{\eta}^5(s,t)$, $\boldsymbol{\eta}^6(s,t)$) stands for $(\partial^2_{st} x,\, \partial^2_{st} y)^\top$ (resp., $(\partial^2_{ss} x,\, \partial^2_{ss} y)^\top$, $(\partial^2_{tt} x,\, \partial^2_{tt} y)^\top$) evaluated at the point (s,t), and $Hess_{x,y} u^G(x,y)$ is the 2×2 Hessian matrix of u^G with respect to the global physical variables x, y, evaluated at (x,y).

Proof. Indeed, we have

$$\begin{aligned} \partial^2_{st}\, u^L &= \partial_s \left[\partial_x\, u^G\, \partial_t\, x \,+\, \partial_y\, u^G\, \partial_t\, y \right] \\ &= \partial_s(\partial_x\, u^G)\, \partial_t\, x + \partial_x\, u^G\, \partial^2_{st}\, x \,+\, \partial_s(\partial_y\, u^G)\, \partial_t\, y + \partial_y\, u^G\, \partial^2_{st}\, y \end{aligned}$$

with

$$\partial_s(\partial_x\, u^G) = \partial^2_{xx}\, u^G\, \partial_s\, x \,+\, \partial^2_{xy}\, u^G\, \partial_s\, y,$$

$$\partial_s(\partial_y\, u^G) = \partial^2_{xy}\, u^G\, \partial_s\, x \,+\, \partial^2_{yy}\, u^G\, \partial_s\, y.$$

Similarly, for $\partial^2_{ss} u^L(s,t)$ and $\partial^2_{tt} u^L(s,t)$ we obtain, respectively,

$$\begin{aligned} \partial^2_{ss}\, u^L &= \partial_s \left[\partial_x\, u^G\, \partial_s\, x \,+\, \partial_y\, u^G\, \partial_s\, y \right] \\ &= \partial_s(\partial_x\, u^G)\, \partial_s\, x + \partial_x\, u^G\, \partial^2_{ss}\, x \,+\, \partial_s(\partial_y\, u^G)\, \partial_s\, y + \partial_y\, u^G\, \partial^2_{ss}\, y \end{aligned}$$

$$\begin{aligned} \partial^2_{tt}\, u^L &= \partial_t \left[\partial_x\, u^G\, \partial_t\, x \,+\, \partial_y\, u^G\, \partial_t\, y \right] \\ &= \partial_t(\partial_x\, u^G)\, \partial_t\, x + \partial_x\, u^G\, \partial^2_{tt}\, x \,+\, \partial_t(\partial_y\, u^G)\, \partial_t\, y + \partial_y\, u^G\, \partial^2_{tt}\, y, \end{aligned}$$

with

$$\partial_t(\partial_x\, u^G) = \partial^2_{xx}\, u^G\, \partial_t\, x \,+\, \partial^2_{xy}\, u^G\, \partial_t\, y,$$

$$\partial_t(\partial_y\, u^G) = \partial^2_{xy}\, u^G\, \partial_t\, x \,+\, \partial^2_{yy}\, u^G\, \partial_t\, y,$$

thus the result, by relying on the expressions of $\boldsymbol{\eta}^5(s,t)$ and $\boldsymbol{\eta}^6(s,t)$. □

To find the expression of the second order derivatives of u^G with respect to the local variables x, y, we may consider the mathematical expressions in Lemma 2 as three equations of a algebraic linear system $M\mathbf{z} = \mathbf{b}$. The vector of unknowns $\mathbf{z}$ has components $\partial^2_{xy} u^G$, $\partial^2_{xx} u^G$, $\partial^2_{yy} u^G$, hidden in the Hessian matrix $Hess_{x,y} u^G(x,y)$, and the matrix M has entries which depend on the products $\boldsymbol{\eta}^2(s,t) \otimes \boldsymbol{\eta}^2(s,t)$, $\boldsymbol{\eta}^2(s,t) \otimes \boldsymbol{\eta}^3(s,t)$ and $\boldsymbol{\eta}^3(s,t) \otimes \boldsymbol{\eta}^3(s,t)$. Finally, the right-hand side $\mathbf{b}$ is the vector with components given by the difference between the entries $\partial^2_{st} u^L$, $\partial^2_{ss} u^L$, $\partial^2_{tt} u^L$, and the corresponding terms containing $\boldsymbol{\eta}^4(s,t)$, $\boldsymbol{\eta}^5(s,t)$, $\boldsymbol{\eta}^6(s,t)$, respectively.

4 | COUPLED DISCRETE PROBLEM AND RESOLUTION.

The meshes τ_H in Ω_H and τ_h in ω_h do not match neither at Γ nor at γ. The associated discrete spaces with no boundary conditions are denoted by $\mathcal{V}_H$, $\mathcal{V}_h$, respectively, and we set $\mathcal{V}_{0,H} = \mathcal{V}_H \cap H^1_0(\Omega_H)$ and $\mathcal{V}_{0,h} = \mathcal{V}_h \cap H^1_0(\omega_h)$ those taking into account homogeneous

boundary Dirichlet conditions on $\partial\Omega_H$ and $\partial\omega_h$, respectively. The trace space of $\mathcal{V}_H$ on Γ (resp., of $\mathcal{V}_h$ on γ) is called $\mathcal{W}_H(\Gamma)$ (resp., $\mathcal{W}_h(\gamma)$). We note that neither the restriction of a function $v_H \in \mathcal{V}_H$ onto the interface γ is, in general, an element of $\mathcal{W}_h(\gamma)$, nor the restriction of $w_h \in \mathcal{V}_h$ onto Γ, is in $\mathcal{W}_H(\Gamma)$. Hence, the Dirichlet problems on $\mathcal{V}_H$ and $\mathcal{V}_h$, respectively, cannot be solved directly, and two suitable operators

$$\Pi_h : H^1(\Omega_H) \longrightarrow \mathcal{W}_h(\gamma)\,, \qquad \Pi_H : H^1(\omega_h) \longrightarrow \mathcal{W}_H(\Gamma),$$

are required, that we define later.

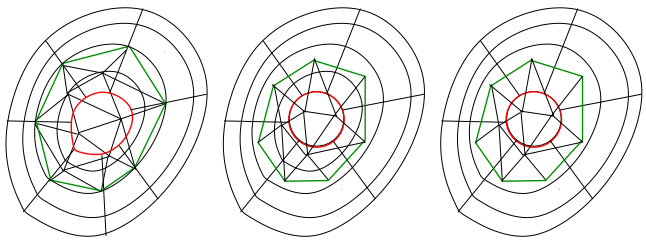

Figure 6 Curved quadrilaterals in Ω_H and straight triangles in ω_h. The mesh of triangles can be built in such a way that either the vertices on γ coincide with quadrilateral vertices on Γ (left) or not (center and right). The size $\delta = \mathrm{dist}(\Gamma, \gamma)$ of the overlap between Ω_H and ω_h is either large when $\delta \geq \min(h, H)$ (left and center) or small when $\delta \leq \max(h, H)$ (right).

We can now formulate the discrete version of problem (2) as follows. Find $(u_H, u_h) \in \mathcal{X}_H \times \mathcal{X}_h$ with $(u_H)_{|\partial D} = g_H$, such that, for all $(v, w) \in \mathcal{X}_{0,H} \times \mathcal{X}_{0,h}$, we have

$$a_{\Omega_H}(u_H, v) + a_{\omega_h}(u_h, w) = (f_{|\Omega_H}, v)_{\Omega_H} + (f_{|\omega_h}, w)_{\omega_h}, \tag{11}$$

with $\mathcal{X}_H = \{v \in \mathcal{V}_H,\, v_{|\Gamma} = \Pi_H u_h\}$ and $\mathcal{X}_h = \{w \in \mathcal{V}_h,\, w_{|\gamma} = \Pi_h u_H\}$ (the functions in the spaces $\mathcal{X}_{0,H}$ and $\mathcal{X}_{0,h}$ take zero boundary values). The finite element solution u^* is defined by

$$u^* = \begin{cases} u_H & \text{in } \Omega_H, \\ u_h & \text{in } \omega_h. \end{cases}$$

In general $u^* \notin H^1(D)$. The error $e = u - u^*$ measured in the broken H^1-norm $||.||_*^2 = ||.||_{1,\Omega_H}^2 + ||.||_{1,\omega_h}^2$ is thus $||e||_*^2 = ||u - u_H||_{1,\Omega_H}^2 + ||u - u_h||_{1,\omega_h}^2$. We expect to have $||e||_{1,\Omega_H \cup \omega_h}$ globally behaving as $O(h^2)$ since cubic or bi-cubic $\mathcal{C}^1$-FEs are used in the subdomains. In this work, we will compute the solution of (11) iteratively, by a one-level alternating Schwarz method [15]. This choice is dictated by simplicity in future applications to plasma simulations.

Let k be the iteration index. Given a guess for $u_h^{(k)}$ in ω_h (actually, we only need values along γ at the initial iteration $k = 0$), solve, for $k \geq 0$, the boundary value problems

$$\begin{aligned} a_{\Omega_H}(u_H^{(k+1)}, v) &= (f_{|\Omega_H}, v) \;\; \forall\, v \in \mathcal{V}_{0,H}, \\ u_H^{(k+1)} &= g \qquad\qquad \text{on } \partial\Omega_H \setminus \Gamma, \\ u_H^{(k+1)} &= \Pi_H\, u_h^{(k)} \quad \text{on } \Gamma, \end{aligned} \tag{12}$$

for $u_H^{(k+1)} \in \mathcal{V}_H$ and this other problem

$$\begin{aligned} a_{\omega_h}(u_h^{(k+1)}, w) &= (f_{|\omega_h}, w) \quad \forall\, w \in \mathcal{V}_{0,h}, \\ u_h^{(k+1)} &= g \qquad\qquad \text{on } \partial\omega_h \setminus \gamma, \\ u_h^{(k+1)} &= \Pi_h\, u_H^{(k+1)} \quad \text{on } \gamma, \end{aligned} \tag{13}$$

for $u_h^{(k+1)} \in \mathcal{V}_h$ (if $\omega_h \subset \Omega_H$, then $\partial\omega_h \setminus \gamma = \emptyset$). The two discrete boundary value problems (12), (13), have a unique solution $u_H^{(k+1)}$, $u_h^{(k+1)}$, respectively, for each $k \geq 0$. At each step k, $u_H^{(k+1)}$ is the approximated discrete solution in Ω_H and $u_h^{(k+1)}$ is the approximated discrete solution for ω_h. In the overlapping region, one is free to use either of the two solutions, since both solutions will converge to the same value in the shared region, as the mesh is refine. In[16,17], a mortar finite element method on overlapping subdomains for solving two-dimensional elliptic problems discretized on composite grids is presented and analyzed. For classical FEs, they prove an optimal error bound and estimate the condition numbers of certain overlapping Schwarz preconditioned systems for the two-subdomain case. In[18], we can find an approach similar to algorithm (12)-(13), involving again $\mathcal{C}^0$ low-order piece-wise (linear or bilinear) FEs in Ω_H and ω_h, coupled by mortar like projections on Γ, γ. The proof of convergence relies on a discrete maximum principle (DMP), appeared in[19], and on the fact that local approximations are piece-wise linear polynomials. For $\mathcal{C}^0$ Lagrange FEs of polynomial degree $r \geq 2$, the DMP does not hold, see[19], and much less is known for $\mathcal{C}^1$ non-Lagrange FEs as the ones used here. We thus work on the numerical side. In the next section, we state the matrix form of (12)-(13), by replacing v in (12) (resp. w in (13)) with the basis functions $\{\psi_s\}$ (resp. $\{\phi_p\}$) for the corresponding discrete space $\mathcal{V}_{0,H}$ (resp. $\mathcal{V}_{0,h}$). The coupling conditions on Γ and γ are realized by interpolation. To perform the convergence analysis of the adopted algorithm we see it as a block Gauss-Seidel method for a linear system that contains the discretization of both subdomains and the coupling along Γ and γ. The convergence of $u_H^{(k)}$ yields that of $u_h^{(k)}$.

4.1 | Matrix form

Let $\mathbf{u}^{\triangle}$ (resp., $\mathbf{u}^{\square}$) the vector gathering all dofs of u_h (resp., of u_H) at the mesh nodes in τ_h (resp., in τ_H). We can separate $\mathbf{u}^{\triangle}$, and analogously $\mathbf{u}^{\square}$, into three blocks, as follows

$$\mathbf{u}^{\triangle} = \begin{pmatrix} \mathbf{u}_{\circ}^{\triangle} \\ \\ \mathbf{u}_{\partial}^{\triangle} \\ \\ \mathbf{u}_{\Gamma}^{\triangle} \end{pmatrix} \qquad \begin{aligned} &\longleftarrow \text{ dofs at } \mathbf{x} \in \mathring{\Omega}_H \text{ thus } \mathbf{x} \notin \partial\Omega_H, \\ &\longleftarrow \text{ dofs at } \mathbf{x} \in \partial\Omega_H \text{ but } \mathbf{x} \notin \Gamma, \\ &\longleftarrow \text{ dofs at } \mathbf{x} \in \Gamma. \end{aligned}$$

The block $\mathbf{u}_{\partial}^{\square}$ is actually known since it is given by the Dirichlet boundary condition, but it is kept as unknown in order to simplify the presentation. Similarly, the block $\mathbf{u}_{\partial}^{\triangle}$ may be not necessary if $\omega_h \subset \Omega_H$. Note that with the functions f and g are associated the vectors $\mathbf{f}^{\square}$, $\mathbf{f}^{\triangle}$, $\mathbf{g}^{\square}$, $\mathbf{g}^{\triangle}$, with structure similar to that of $\mathbf{u}^{\square}$ and $\mathbf{u}^{\triangle}$. Here, we have $(\mathbf{g}_{\circ}^{\square}, \mathbf{g}_{\Gamma}^{\square}) = (\mathbf{0}, \mathbf{0})$ and $(\mathbf{g}_{\circ}^{\triangle}, \mathbf{g}_{\gamma}^{\triangle}) = (\mathbf{0}, \mathbf{0})$. Let $A^{\square}$ (resp., $A^{\triangle}$) be the matrix associated with the operator $\mathcal{L}$ restricted to τ_H (resp., τ_h) and

$$\mathbf{u}_{\Gamma}^{\square} = P_{\Gamma\circ}\mathbf{u}_{\circ}^{\triangle} + P_{\Gamma\gamma}\mathbf{u}_{\gamma}^{\triangle}, \qquad\qquad \mathbf{u}_{\gamma}^{\triangle} = \widehat{P}_{\gamma\circ}\mathbf{u}_{\circ}^{\square} + \widehat{P}_{\gamma\Gamma}\mathbf{u}_{\Gamma}^{\square},$$

are, respectively, those of the operators Π_H (the first relation) and Π_h (the second relation). To indicate that the interior block, denoted by $\circ$, which appears in $\widehat{P}_{\gamma\circ}$ is different from the one in $P_{\Gamma\circ}$, we have introduced a wide hat. Numerical experiments in[14] hint that the direct coupled problem solution u^* becomes unstable due to over-imposing continuity at the interfaces when the overlap, $\delta = \mathrm{dist}(\Gamma, \gamma)$, is small (namely, $\delta \leq \min(h, H)$, as for example in Fig. 6 right). In the following, we thus work under Assumption 1.

Assumption 1. The size δ of the overlapping region, $\Omega_H \cap \omega_h$, is large, that means, $P^{\square}_{\Gamma\gamma} = 0$ and $\widehat{P}_{\gamma\Gamma} = 0$.

We detail the construction of the blocks $\widehat{P}_{\gamma\circ}$ and $P_{\Gamma\circ}$.

4.1.1 | The coupling operator Π_h

We proceed by interpolation. The construction of Π_h relies on the identities (8) (with $\eta^1 = 1$) and (10), to pass the information, on the field value and derivatives, respectively, from an element $Q_e \in \tau_H$ to its internal node $\mathbf{X}^* \in \gamma$. This operation needs to determine $(s^*, t^*) \in \hat{Q}$ such that $(s^*, t^*) = F_e^{-1}(\mathbf{X}^*)$ with F_e the bi-cubic transformation (5) associated with Q_e. Note that F_e can be inverted, for example, by a Newton iterative algorithm. However, in this work, we assume for simplicity that the nodes on γ belong also to τ_H (see Fig. 6, left). In other words, each node $\mathbf{X}^* \in \gamma$ has a global number ℓ^* in τ_h and i^* in τ_H. When $\mathbf{X}^*$ is a vertex of an element $Q^e \in \tau_H$, we have that (s^*, t^*) is either $(0, 0)$, or $(1, 0)$, $(1, 1)$, $(0, 1)$. Each node in τ_h (τ_H) is associated with 3 (4) types j of dofs. If we detail the matrix expression of Π_h interpolating u_h at $\mathbf{X}^*$ starting from u_H, we have

$$(\mathbf{u}^{\triangle}_{\gamma})_{\ell^*} = (\widehat{P}_{\gamma\circ})_{\ell^* i^*} \, (\mathbf{u}^{\square}_{\circ})_{i^*}$$

with the 3×4 matrix

$$(\widehat{P}_{\gamma\circ})_{\ell^* i^*} = \begin{pmatrix} 1 & 0 & 0 & 0 \\ 0 & (\partial_t y)/|J| & -(\partial_s y)/|J| & 0 \\ 0 & -(\partial_t x)/|J| & (\partial_t x)/|J| & 0 \end{pmatrix}$$

evaluated at (s^*, t^*), where $|J| = \det J(s^*, t^*)$. The entries of row/column 1 of $(P_{\gamma\circ})_{\ell^* i^*}$ come from (8) and those of the row/column 2 and 3 are the entries of matrix $(J(s^*, t^*)^\top)^{-1}$, according to (10). Finally

$$(\mathbf{u}^{\triangle}_{\gamma})_{\ell^*} = (v \, , \, \partial_x v \, , \, \partial_y v)^\top \, (\mathbf{X}^*), \qquad (\mathbf{u}^{\square}_{\circ})_{i^*} = \left(\hat{z} \, , \, \partial_s \hat{z} \, , \, \partial_t \hat{z} \, , \, \partial^2_{st} \hat{z}\right)^\top (s^*, t^*),$$

with $v \in \mathcal{V}_h$, $\hat{z}(.) = z(F_e^{-1}(.))$ for $z \in \mathcal{V}_H$. Note that the same values in the vector $(\mathbf{u}^{\square}_{\circ})_{i^*}$ can be computed starting from $(s^*, t^*) = F_e^{-1}(\mathbf{X}^*)$ with F_e associated with any Q_e among the 4 elements with a vertex in $\mathbf{X}^*$, since the HB FE is of class $\mathcal{C}^1$.

4.1.2 | The coupling operator Π_H

We proceed again by interpolation. The construction of Π_H uses the identities (8) (with $\eta^1 = 1$) and (9) to transfer the information, on the field value and derivatives, respectively, from an element $T_e \in \tau_h$ to a node $\mathbf{X}^\star \in \Gamma$. To find which $T_e \in \tau_h$ contains $\mathbf{X}^\star$, we compute

the barycentric coordinates $\lambda_v(\mathbf{X}^\star)$ with respect to the vertices of T_e and verify that $0 \le \lambda_p(\mathbf{X}^\star) \le 1$ for all $p = 1, 2, 3$. If we detail the matrix expression of Π_H interpolating u_H at $\mathbf{X}^\star$ starting from u_h, we have

$$(\mathbf{u}_\Gamma^\square)_{i^\star} = (P_{\Gamma\circ})_{i^\star \ell^\star}\, (\mathbf{u}_\circ^\triangle)_{\ell^\star}$$

with the 4×3 matrix

$$(P_{\Gamma\circ})_{i^\star \ell^\star} = \begin{pmatrix} 1 & 0 & 0 \\ 0 & \partial_s x & \partial_s y \\ 0 & \partial_t x & \partial_t y \\ 0 & 0 & 0 \end{pmatrix}$$

evaluated at $(s^\star, t^\star)$. Note that $(s^\star, t^\star)$ coincides with either $(0,0)$, or $(1,0)$, $(1,1)$, $(0,1)$ depending on the local coordinates of $\mathbf{X}^\star$ in the elements Q_e with a vertex in $\mathbf{X}^\star$ and an edge on Γ. The entries of row/column 1 of $(P_{\Gamma\circ})_{i^\star \ell_p^\star}$ come from (8) and those of the row/column 2 and 3 are the entries of matrix $J(s^\star, t^\star)$, according to (9). Finally

$$(\mathbf{u}_\Gamma^\square)_{i^\star} = \left(\hat{z}\,,\, \partial_s \hat{z}\,,\, \partial_t \hat{z}\,,\, \partial^2_{st} \hat{z}\right)^\top (s^\star, t^\star), \qquad (\mathbf{u}_\circ^\triangle)_{\ell^\star} = (v\,,\, \partial_x v\,,\, \partial_y v)^\top (\mathbf{X}^\star),$$

with $\hat{z} \in P_{loc}(\hat{Q})$ and v, $\partial_x v$, $\partial_y v$ computed at $\mathbf{X}^\star$ from the rHCT dofs associated with the vertices of the triangle T_e containing $\mathbf{X}^\star$.

Remark 1. If the coupling operators $\Pi_H : H^1(\omega_h) \to \mathcal{W}_H(\Gamma)$ and $\Pi_h : H^1(\Omega_H) \to \mathcal{W}_h(\gamma)$ are L^2 projections on the trace spaces $\mathcal{W}_H(\Gamma)$, $\mathcal{W}_h(\gamma)$, respectively, we have

$$P_{\Gamma\circ} = (M_{\Gamma\Gamma}^\square)^{-1}\, C_{\Gamma\circ}, \quad \widehat{P}_{\gamma\circ} = (M_{\gamma\gamma}^\triangle)^{-1}\, \widehat{C}_{\gamma\circ}$$

where $M_{\Gamma\Gamma}^\square$ (resp., $M_{\gamma\gamma}^\triangle$) is a square matrix in Ω_H (resp. in ω_h) computed by involving basis functions associated with unknowns on Γ (resp., on γ), whereas $\widehat{C}_{\gamma\circ}$ (resp. $C_{\Gamma\circ}$) is a rectangular of size $N_\gamma^\triangle \times N_\circ^\square$ (resp. $N_\Gamma^\square \times N_\circ^\triangle$). In detail,

$$(M_{\Gamma\Gamma}^\square)_{pq} = \int_\Gamma \varphi_p^\square\, \varphi_q^\square, \qquad (C_{\Gamma\circ})_{p\ell} = \int_\Gamma \varphi_p^\square\, \psi_\ell^\triangle,$$

$$(M_{\gamma\gamma}^\triangle)_{\hat{p}\hat{q}} = \int_\gamma \psi_{\hat{p}}^\triangle\, \psi_{\hat{q}}^\triangle, \quad (\widehat{C}_{\gamma\circ})_{\hat{p}k} = \int_\gamma \psi_{\hat{p}}^\triangle\, \varphi_k^\square,$$

with p, q global numbers of dofs associated with nodes on Γ; $\hat{p}, \hat{q}$ global numbers of dofs associated with nodes on γ; ℓ in the block of $N_\circ^\triangle$ dofs associated with points in ω_h, but not on γ, and k in the block of $N_\circ^\square$ dofs associated with points in Ω_H, but not on Γ. The integrals above are computed by means of quadrature rules. As already remarked and illustrated in Figure 7, the operation of localizing the (quadrature) points of γ at the interior of the curved elements in τ_H is not easy (we have to invert a bi-cubic mapping, for each of the quadrature points). Such a type of projections is well-known from the mortar finite element context (see,[20]). The convergence of multidomain approximations with overlap of arbitrary finite element meshes in the case of the mortar element method is firstly analyzed in[16,21].

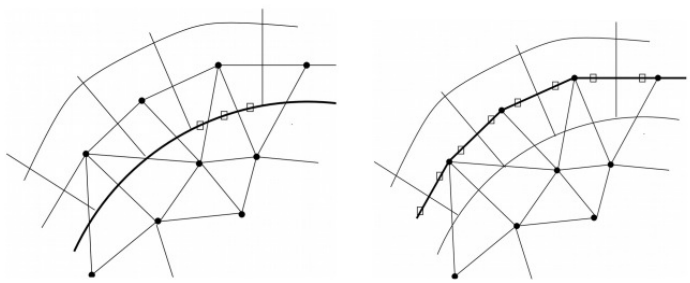

Figure 7 Curved quadrilaterals in Ω_H and straight triangles in ω_h, in a simplified situation. On the left, each quadrature node (indicated by a $\square$) on Γ (thick solid line) can be localized in a triangles $T \in \tau_h$ by relying on the values of the barycentric coordinates $\lambda_v(\square)$, being v the vertices of T (indicated by $\bullet$). On the right, we need to use a Newton algorithm to localize each quadrature node ($\square$) on γ (thick solid line) inside a curved quadrangle $Q \in \tau_H$.

4.2 | Convergence analysis

For each problem matrix, we need to build the three blocks $A_{\circ\circ}$, $A_{\circ\partial}$ and $A_{\circ I}$ where: $A_{\circ\circ}$ represents the coupling between dofs associated with nodes at the interior of the mesh, $A_{\circ\partial}$ represents the coupling between dofs associated with nodes at the interior of the mesh and dofs at nodes on Dirichlet-type boundaries, and $A_{\circ I}$ represents the coupling between dofs associated with nodes at the interior of the mesh and dofs at nodes lying on the coupling interface (I stands for either γ or Γ). Under Assumption 1, the matrix form of problem (12)-(13) reads: starting from $\mathbf{u}^{\triangle,(k)}$, we can first compute $\mathbf{u}^{\square,(k+1)}$ and then $\mathbf{u}^{\triangle,(k+1)}$ by solving successively

$$\begin{aligned} A^{\square}_{\circ\circ}\,\mathbf{u}^{\square,(k+1)}_{\circ} + A^{\square}_{\circ\Gamma}\,P_{\Gamma\circ}\,\mathbf{u}^{\triangle,(k)}_{\circ} &= \tilde{\mathbf{f}}^{\square}_{\circ}, \\ A^{\triangle}_{\circ\circ}\,\mathbf{u}^{\triangle,(k+1)}_{\circ} + A^{\triangle}_{\circ\gamma}\,\widehat{P}_{\gamma\circ}\,\mathbf{u}^{\square,(k+1)}_{\circ} &= \tilde{\mathbf{f}}^{\triangle}_{\circ} \end{aligned} \tag{14}$$

where $\tilde{\mathbf{f}}^{\square}_{\circ} = \mathbf{f}^{\square}_{\circ} - A^{\square}_{\circ\partial}\,\mathbf{g}^{\square}_{\partial}$ and $\tilde{\mathbf{f}}^{\triangle}_{\circ} = \mathbf{f}^{\triangle}_{\circ} - A^{\triangle}_{\circ\partial}\,\mathbf{g}^{\triangle}_{\partial}$, respectively. Algorithm (14) is a block Gauss-Seidel method to find vectors $\mathbf{u}^{\square}$ and $\mathbf{u}^{\triangle}$ solution of the linear system

$$\begin{pmatrix} A^{\square}_{\circ\circ} & A^{\square}_{\circ\Gamma}\,P_{\Gamma\circ} \\ A^{\triangle}_{\circ\gamma}\,\widehat{P}_{\gamma\circ} & A^{\triangle}_{\circ\circ} \end{pmatrix} \begin{pmatrix} \mathbf{u}^{\square}_{\circ} \\ \mathbf{u}^{\triangle}_{\circ} \end{pmatrix} = \begin{pmatrix} \tilde{\mathbf{f}}^{\square}_{\circ} \\ \tilde{\mathbf{f}}^{\triangle}_{\circ} \end{pmatrix}. \tag{15}$$

The other way around, being system (15) equivalent to

$$\begin{pmatrix} A^{\triangle}_{\circ\circ} & A^{\triangle}_{\circ\gamma}\,\widehat{P}_{\gamma\circ} \\ A^{\square}_{\circ\Gamma}\,P_{\Gamma\circ} & A^{\square}_{\circ\circ} \end{pmatrix} \begin{pmatrix} \mathbf{u}^{\triangle}_{\circ} \\ \mathbf{u}^{\square}_{\circ} \end{pmatrix} = \begin{pmatrix} \tilde{\mathbf{f}}^{\triangle}_{\circ} \\ \tilde{\mathbf{f}}^{\square}_{\circ} \end{pmatrix}, \tag{16}$$

we can start from $\mathbf{u}^{\square,(k)}$, compute $\mathbf{u}^{\triangle,(k+1)}$ and then $\mathbf{u}^{\square,(k+1)}$, by solving successively

$$\begin{aligned} A^{\triangle}_{\circ\circ}\,\mathbf{u}^{\triangle,(k+1)}_{\circ} + A^{\triangle}_{\circ\gamma}\,\widehat{P}_{\gamma\circ}\,\mathbf{u}^{\square,(k)}_{\circ} &= \tilde{\mathbf{f}}^{\triangle}_{\circ}, \\ A^{\square}_{\circ\circ}\,\mathbf{u}^{\square,(k+1)}_{\circ} + A^{\square}_{\circ\Gamma}\,P_{\Gamma\circ}\,\mathbf{u}^{\triangle,(k+1)}_{\circ} &= \tilde{\mathbf{f}}^{\square}_{\circ}. \end{aligned} \tag{17}$$

Note that even if the matrix of the linear system (15) has symmetric diagonal blocks it is globally non-symmetric since $A^{\triangle}_{\circ\gamma}\,\widehat{P}_{\gamma\circ} \neq (A^{\square}_{\circ\Gamma}\,P_{\Gamma\circ})^t$. When dealing with such general matrices, no a priori conclusions on the convergence properties of the Gauss-Seidel method

can be drawn. We address the problem of estimating the error introduced by the iterative method and on the reduction factor of the error at each iteration. The diagonal blocks $A^{\triangle}_{\circ\circ}$, $A^{\square}_{\circ\circ}$, can be inverted since the subdomain discrete problems, (12) in $\mathcal{V}_H$ and (13) in $\mathcal{V}_h$, have a unique solution, separately, by treating Γ and γ as Dirichlet boundaries.

Lemma 3. Algorithm (14) with $\mathbf{u}^{\triangle,(0)}_{\circ} = (A^{\triangle}_{\circ\circ})^{-1}\tilde{\mathbf{f}}^{\triangle}_{\circ}$ yields the following recursive definition of $\mathbf{u}^{\triangle,(k+1)}_{\circ}$, for $k \geq 1$:

$$(\mathbf{u}^{\triangle,(k+1)}_{\circ} - \mathbf{u}^{\triangle,(k)}_{\circ}) \;= (A^{\triangle}_{\circ\circ})^{-1} A^{\triangle}_{\circ\gamma}\, \widehat{P}_{\gamma\circ}\, (A^{\square}_{\circ\circ})^{-1} A^{\square}_{\circ\Gamma}\, P_{\Gamma\circ}\, (\mathbf{u}^{\triangle,(k)}_{\circ} - \mathbf{u}^{\triangle,(k-1)}_{\circ}). \tag{18}$$

Proof. We start from the first line of (14) and compute $\mathbf{u}^{\square,(k+1)}_{\circ}$, namely

$$\begin{aligned}
\mathbf{u}^{\square,(k+1)}_{\circ} &= (A^{\square}_{\circ\circ})^{-1}[\tilde{\mathbf{f}}^{\square}_{\circ} - A^{\square}_{\circ\Gamma}\, P_{\Gamma\circ}\, \mathbf{u}^{\triangle,(k)}_{\circ}] \\
&= (A^{\square}_{\circ\circ})^{-1}[\tilde{\mathbf{f}}^{\square}_{\circ} - A^{\square}_{\circ\Gamma}\, P_{\Gamma\circ}\, \mathbf{u}^{\triangle,(k-1)}_{\circ} + A^{\square}_{\circ\Gamma}\, P_{\Gamma\circ}\, \mathbf{u}^{\triangle,(k-1)}_{\circ} - A^{\square}_{\circ\Gamma}\, P_{\Gamma\circ}\, \mathbf{u}^{\triangle,(k)}_{\circ}] \\
&= (A^{\square}_{\circ\circ})^{-1}[\tilde{\mathbf{f}}^{\square}_{\circ} - A^{\square}_{\circ\Gamma}\, P_{\Gamma\circ}\, \mathbf{u}^{\triangle,(k-1)}_{\circ}] - (A^{\square}_{\circ\circ})^{-1} A^{\square}_{\circ\Gamma}\, P_{\Gamma\circ}\, (\mathbf{u}^{\triangle,(k)}_{\circ} - \mathbf{u}^{\triangle,(k-1)}_{\circ}) \\
&= \mathbf{u}^{\square,(k)}_{\circ} - (A^{\square}_{\circ\circ})^{-1} A^{\square}_{\circ\Gamma}\, P_{\Gamma\circ}\, (\mathbf{u}^{\triangle,(k)}_{\circ} - \mathbf{u}^{\triangle,(k-1)}_{\circ}),
\end{aligned}$$

where we set $\mathbf{u}^{\triangle,(-1)}_{\circ} = \mathbf{0}$. We thus use $\mathbf{u}^{\square,(k+1)}_{\circ}$ in the second line of (14),

$$\begin{aligned}
\mathbf{u}^{\triangle,(k+1)}_{\circ} &= (A^{\triangle}_{\circ\circ})^{-1}\left[\tilde{\mathbf{f}}^{\triangle}_{\circ} - A^{\triangle}_{\circ\gamma}\, \widehat{P}_{\gamma\circ}\, \mathbf{u}^{\square,(k+1)}_{\circ}\right] \\
&= (A^{\triangle}_{\circ\circ})^{-1}\left[\tilde{\mathbf{f}}^{\triangle}_{\circ} - A^{\triangle}_{\circ\gamma}\, \widehat{P}_{\gamma\circ}\, [\mathbf{u}^{\square,(k)}_{\circ} - (A^{\square}_{\circ\circ})^{-1} A^{\square}_{\circ\Gamma}\, P_{\Gamma\circ}\, (\mathbf{u}^{\triangle,(k)}_{\circ} - \mathbf{u}^{\triangle,(k-1)}_{\circ})]\right] \\
&= \mathbf{u}^{\triangle,(k)}_{\circ} + (A^{\triangle}_{\circ\circ})^{-1} A^{\triangle}_{\circ\gamma}\, \widehat{P}_{\gamma\circ}\, (A^{\square}_{\circ\circ})^{-1} A^{\square}_{\circ\Gamma}\, P_{\Gamma\circ}\, (\mathbf{u}^{\triangle,(k)}_{\circ} - \mathbf{u}^{\triangle,(k-1)}_{\circ}),
\end{aligned}$$

which is the desired recursion (18). □

Lemma 4. Algorithm (17) with $\mathbf{u}^{\square,(0)}_{\circ} = (A^{\square}_{\circ\circ})^{-1}\tilde{\mathbf{f}}^{\square}_{\circ}$ yields the following recursive definition of $\mathbf{u}^{\square,(k+1)}_{\circ}$, for $k \geq 1$:

$$(\mathbf{u}^{\square,(k+1)}_{\circ} - \mathbf{u}^{\square,(k)}_{\circ}) \;= (A^{\square}_{\circ\circ})^{-1} A^{\square}_{\circ\Gamma}\, P_{\Gamma\circ}\, (A^{\triangle}_{\circ\circ})^{-1} A^{\triangle}_{\circ\gamma}\, \widehat{P}_{\gamma\circ}\, (\mathbf{u}^{\square,(k)}_{\circ} - \mathbf{u}^{\square,(k-1)}_{\circ}). \tag{19}$$

Proof. Similarly to the proof of Lemma 3, we start from the first line of (17) and compute $\mathbf{u}^{\triangle,(k+1)}_{\circ}$. We thus use $\mathbf{u}^{\triangle,(k+1)}_{\circ}$ in the second line of (17). □

Let us introduce the matrix $\mathcal{A} = (A^{\square}_{\circ\circ})^{-1} A^{\square}_{\circ\Gamma}\, P_{\Gamma\circ}$, of size $N^{\square}_{\circ} \times N^{\triangle}_{\circ}$, and the matrix $\mathcal{B} = (A^{\triangle}_{\circ\circ})^{-1} A^{\triangle}_{\circ\gamma}\, \widehat{P}_{\gamma\circ}$, of size $N^{\triangle}_{\circ} \times N^{\square}_{\circ}$, respectively. We see that (18) and (19) can be written, respectively, as follows

$$(\mathbf{u}^{\triangle,(k+1)}_{\circ} - \mathbf{u}^{\triangle,(k)}_{\circ}) = \mathcal{B}\,\mathcal{A}\,(\mathbf{u}^{\triangle,(k)}_{\circ} - \mathbf{u}^{\triangle,(k-1)}_{\circ}),$$

$$(\mathbf{u}^{\square,(k+1)}_{\circ} - \mathbf{u}^{\square,(k)}_{\circ}) = \mathcal{A}\,\mathcal{B}\,(\mathbf{u}^{\square,(k)}_{\circ} - \mathbf{u}^{\square,(k-1)}_{\circ}).$$

The matrices $\mathcal{A}$ and $\mathcal{B}$ are, in general, rectangular. However, the non-zero eigenvalues of $\mathcal{A}\mathcal{B}$ are the same as those of $\mathcal{B}\mathcal{A}$. Indeed, let $\mu \neq 0$ be an eigenvalue of $\mathcal{A}\mathcal{B}$. Then, it exists a non-zero vector $\mathbf{w} \in \mathbb{R}^m$ with $m = N^{\square}_{\circ}$, such that $\mathcal{A}\mathcal{B}\,\mathbf{w} = \mu\,\mathbf{w}$. Hence,

$$\mathcal{B}\,(\mathcal{A}\mathcal{B}\,\mathbf{w}) = \mathcal{B}\,(\mu\,\mathbf{w}) \quad \Longrightarrow \quad (\mathcal{B}\mathcal{A})\,(\mathcal{B}\,\mathbf{w}) = \mu\,(\mathcal{B}\,\mathbf{w})$$

that is μ is also eigenvalue of $\mathcal{B}\mathcal{A}$ with associated eigenvector $\mathcal{B}\mathbf{w}$. Note that $\mathcal{B}\mathbf{w} \neq \mathbf{0}$ otherwise we would have $\mathcal{A}\mathcal{B}\mathbf{w} = \mu\mathbf{w} = 0$ which yields $\mu = 0$. Algorithm (14) (and (17)) converges if $\rho < 1$, being ρ the spectral radius of the square matrix $\mathcal{A}\mathcal{B}$ (or, equivalently, $\mathcal{B}\mathcal{A}$, as stated before).

Lemma 5. System (16) has a unique solution iff $(I - \mathcal{A}\mathcal{B})$ is nonsingular.

Proof. Let us write the matrix $\mathcal{G}$ of the linear system (16) as $\mathcal{G} = \mathcal{M} + \mathcal{N}$, with

$$\mathcal{M} = \begin{pmatrix} A^{\triangle}_{\circ\circ} & 0 \\ A^{\square}_{\circ\Gamma} P_{\Gamma\circ} & A^{\square}_{\circ\circ} \end{pmatrix}, \qquad \mathcal{N} = \begin{pmatrix} 0 & A^{\triangle}_{\circ\gamma} \widehat{P}_{\gamma\circ} \\ 0 & 0 \end{pmatrix}.$$

Being $A^{\square}_{\circ\circ}$, $A^{\triangle}_{\circ\circ}$ nonsingular, $\mathcal{M}$ can be inverted and the block structure of its inverse reads

$$\mathcal{M}^{-1} = \begin{pmatrix} (A^{\triangle}_{\circ\circ})^{-1} & 0 \\ -\mathcal{A}(A^{\triangle}_{\circ\circ})^{-1} & (A^{\square}_{\circ\circ})^{-1} \end{pmatrix}.$$

We thus get $\mathcal{M}^{-1}\mathcal{G} = \mathcal{I} + \mathcal{M}^{-1}\mathcal{N}$, that is

$$\mathcal{M}^{-1}\mathcal{G} = \begin{pmatrix} I^{\triangle}_{\circ\circ} & (A^{\triangle}_{\circ\circ})^{-1} A^{\triangle}_{\circ\gamma} \widehat{P}_{\gamma\circ} \\ -\mathcal{A} + \mathcal{A} & I^{\square}_{\circ\circ} - \mathcal{A}\mathcal{B} \end{pmatrix} = \begin{pmatrix} I^{\triangle}_{\circ\circ} & \mathcal{B} \\ 0 & I^{\square}_{\circ\circ} - \mathcal{A}\mathcal{B} \end{pmatrix},$$

and the statement holds true. □

Similarly, we can prove that the linear system (15) has a unique solution iff the matrix $(I - \mathcal{B}\mathcal{A})$ is nonsingular.

Proposition 1. If $(I - \mathcal{A}\mathcal{B})$ is nonsingular, algorithm (17) converges.

Proof. Algorithm (17) reads: find $\mathbf{u}^{\square,(k+1)}_{\circ} \in \mathbb{R}^m$ solution of the linear system

$$\mathbf{u}^{\square,(k+1)}_{\circ} = \mathcal{A}\mathcal{B}\,\mathbf{u}^{\square,(k)}_{\circ} + \mathbf{c}^{\square}, \qquad k \geq 0,$$

with $\mathbf{u}^{\square,(0)}_{\circ} = (A^{\square}_{\circ\circ})^{-1}\,\tilde{\mathbf{f}}^{\square}_{\circ}$ and $\mathbf{c}^{\square} = (A^{\square}_{\circ\circ})^{-1}\,\tilde{\mathbf{f}}^{\square}_{\circ} - \mathcal{A}\,(A^{\triangle}_{\circ\circ})^{-1}\,\tilde{\mathbf{f}}^{\triangle}_{\circ}$. By construction, we have that $\mathbf{u}^{\square}_{\circ} = \mathcal{A}\mathcal{B}\,\mathbf{u}^{\square}_{\circ} + \mathbf{c}^{\square}$. Let $\mathbf{e}^{\square,(k)}_{\circ} = \mathbf{u}^{\square}_{\circ} - \mathbf{u}^{\square,(k)}_{\circ}$ be the error vector at the iteration k. By subtracting the iterate $\mathbf{u}^{\square,(k+1)}_{\circ}$ from $\mathbf{u}^{\square}_{\circ}$, we get

$$\mathbf{e}^{\square,(k+1)}_{\circ} = \mathcal{A}\mathcal{B}\,\mathbf{e}^{\square,(k)}_{\circ}.$$

The matrix $(I - \mathcal{A}\mathcal{B})$ is nonsingular, thus $\rho(\mathcal{A}\mathcal{B}) \neq 1$. To conclude about convergence, it must be $\rho(\mathcal{A}\mathcal{B}) < 1$. Let us prove that

$$||\mathbf{e}^{\square,(k)}_{\circ}||_2 \leq \frac{\sigma}{1-\sigma}\,||\mathbf{u}^{\square,(k)}_{\circ} - \mathbf{u}^{\square,(k-1)}_{\circ}||_2 \tag{20}$$

with σ the largest singular value of the matrix $\mathcal{A}\mathcal{B}$. Indeed, by using (matrix and vector) norm 2 properties, we get

$$||\mathbf{e}^{\square,(k+1)}_{\circ}||_2 \leq \sigma||\,\mathbf{e}^{\square,(k)}_{\circ}||_2 \qquad \sigma = ||\mathcal{A}\mathcal{B}\,||_2 = \sigma_{\max}(\mathcal{A}\mathcal{B}).$$

Table 1 L^2, H^1 and H^2 errors and numerical convergence orders for rHCT FEs on $[0,1]^2$.

nr	L^2 norm	$p_\bullet$	H^1 semi-norm	$p_\bullet$	H^2 semi-norm	$p_\bullet$
3	$9.9885\ \times 10^{-6}$		$1.5106\ \times 10^{-3}$		$3.3870\ \times 10^{-1}$	
6	$1.2031\ \times 10^{-6}$	3.05	$3.7244\ \times 10^{-4}$	2.02	$1.6758\ \times 10^{-1}$	1.01
12	$1.4814\ \times 10^{-7}$	3.02	$9.2608\ \times 10^{-5}$	2.01	$8.3401\ \times 10^{-2}$	1.00
24	$1.8396\ \times 10^{-8}$	3.01	$2.3099\ \times 10^{-5}$	2.00	$4.1611\ \times 10^{-2}$	1.00

We can also write

$$\begin{aligned}
||\mathbf{e}_\circ^{\square,(k)}||_2 &= ||\mathbf{u}_\circ^{\square} - \mathbf{u}_\circ^{\square,(k)}||_2 \\
&= ||\mathbf{u}_\circ^{\square} - \mathbf{u}_\circ^{\square,(k+1)} + \mathbf{u}_\circ^{\square,(k+1)} - \mathbf{u}_\circ^{\square,(k)}||_2 \\
&\leq ||\mathbf{e}_\circ^{\square,(k+1)}||_2 + ||\mathbf{u}_\circ^{\square,(k+1)} - \mathbf{u}_\circ^{\square,(k)}||_2 \\
&\leq \sigma||\,\mathbf{e}_\circ^{\square,(k)}||_2 + \sigma\,||\mathbf{u}_\circ^{\square,(k)} - \mathbf{u}_\circ^{\square,(k-1)}||_2.
\end{aligned}$$

Moving, to the left-side of the inequality, the term $\sigma\,||\mathbf{e}_\circ^{\square,(k)}||_2$, we obtain (20). Inequality (20) yields $\sigma/(1-\sigma) \geq 0$ which can be true only when $0 \leq \sigma < 1$. This yields $\rho(\mathcal{AB}) < 1$, since $\rho \leq \sigma$. Algorithm (17) hence converges. □

5 | NUMERICAL RESULTS

The proposed approach aims at combining HB FEs on a curved and structured quadrilateral mesh in Ω_H and rHCT FEs in ω_h on a straight and unstructured triangular mesh, to treat the singularity at the center of the curved domain Ω_H. We start by checking, separately, the accuracy of the rHCT and HB FEs when adopted to approximate the solution of problem (1) with $\mathcal{L} = -\Delta$. The L^2 norm (resp., the H^1, H^2 semi-norms) of the approximation error is computed by using the expression of u^G (resp., $\nabla_{x,y}u^G$ and the entries of $Hess_{x,y}u^G(x,y)$) given in (7) (resp., after the proofs of Lemmas 1 and 2). We then show an example of coupled approximation on composite meshes. For the considered cases, the matrix $\mathcal{G}$ is nonsingular.

For the rHCT side, we consider the domain $\hat{Q} = [0,1]^2$. Dirichlet boundary function g and right-hand side f are compatible with $u(x,y) = x^4(y-1)^2 + y^4(x-1)^2$ solution of the PDE. In Table 1, we report the numerical errors in the L^2 norm and H^1, H^2 semi-norms together with the convergence orders $p_\bullet$ computed with the rule

$$p_i = log(err_i/err_{i-1})\,/\,log(h_i/h_{i-1}) \qquad i = 2,3,4.$$

We have used different meshes τ with triangles T of size $h_i = \sqrt{2}/(nr)_i$. The theoretical error with rHCT FEs in the L^2 norm (resp., the H^1, H^2 semi-norms) behaves as $O(h^p)$, with $p = 3$ (resp., $p = 2$, $p = 1$) with $h = \max_{T\in\tau} \mathrm{diam}\,(T)$ (see Chapter 4 in[22]), being τ the triangular mesh covering the computational domain, here $\hat{Q}$. We can see that the computed values $p_\bullet$ in Table 1 are close to the corresponding theoretical ones.

Table 2 Error L^2 norm and H^1, H^2 semi-norms (and orders) for HB FEs on R.

nr	L^2 norm	$p_\bullet$	H^1 semi-norm	$p_\bullet$	H^2 semi-norm	$p_\bullet$
6	4.1936×10^{-5}		1.0064×10^{-3}		3.8111×10^{-2}	
12	1.8652×10^{-6}	4.49	9.9291×10^{-5}	3.34	7.6234×10^{-3}	2.32
24	9.9445×10^{-8}	4.23	1.1107×10^{-5}	3.16	1.7170×10^{-3}	2.15
48	5.7550×10^{-9}	4.11	1.3155×10^{-6}	3.08	4.0801×10^{-4}	2.07

Table 3 Error L^2 norm and H^1, H^2 semi-norms (and orders) for HB FEs on D.

nr	L^2 norm	$p_\bullet$	H^1 semi-norm	$p_\bullet$	H^2 semi-norm	$p_\bullet$
12	2.9130×10^{-2}		5.1670×10^{-2}		1.7790×10^{-0}	
24	1.9345×10^{-3}	3.91	5.2603×10^{-3}	3.30	4.5075×10^{-1}	1.98
48	1.3023×10^{-4}	3.89	6.2050×10^{-4}	3.08	1.1470×10^{-1}	1.97
60	5.5449×10^{-5}	3.83	3.1540×10^{-4}	3.03	7.3701×10^{-2}	1.98

For the HB side, we consider either the domain $R = [0.2, 2] \times [0, 1]$ or the curved one $D = \{(r\cos(2\pi\theta), r\sin(2\pi\theta)),\ (r,\theta) \in R\}$. Dirichlet boundary function g and right-hand side f are compatible with $u(x,y) = x^4 + y^3 + x^2y^2$ solution of the PDE. In Tables 2 and 3, we report the numerical errors for HB FEs in the L^2 norm and H^1, H^2 semi-norms together with the convergence orders $p_\bullet$ estimated by the same rule as before. Over the rectangle K, we have used different meshes τ with elements Q of size $h_i \approx 2/(nr)_i$. Over the curved domain D, we have used different curved meshes τ with quadrangles Q of size $h_i \approx 2\pi/(nr)_i$. The theoretical error with HB FEs in the L^2 norm (resp., H^1, H^2 semi-norms) behaves as $O(h^p)$, with $p = 4$ (resp., $p = 3$ and $p = 2$) with $h = \max_{Q\in\tau} \mathrm{diam}(Q)$, being τ the mesh covering either $\overline{R}$ or $\overline{D}$ (see Chapter 4 in [22]). In the HB case over the curved domain D, we have used finer meshes and iso-parametric finite elements (see, for example, Section 5.2 in [23]). We can see that, the computed values $p_\bullet$ in Tables 2 and 3 agree with the corresponding theoretical ones.

We finally consider a coupled test case. Let Ω_H be the annular domain centered at $\mathbf{x}_c = (0,0)$ and $r_{min} = 1.0625$, $r_{max} = 2.375$. Let ω_h be the polygon approximating the disk centered at $\mathbf{x}_c$ and radius $R = 1.375$. Dirichlet boundary function g and right-hand side f are compatible with $u(x,y) = \sin(2.5\pi x)\sin(1.5\pi y)$ solution of the PDE. Adopted meshes and computed solution are shown in Figures 8, 9, respectively.

On the same composite meshes for $\Omega_H \cup \omega_h$, we consider the model PDE with Dirichlet boundary function g and right-hand side f compatible with $u(x,y) = \sin(L_x\pi x)\sin(L_y\pi y)$ as solution. We change L_x and L_y as

$$L_x \in \{0.17\ 0.35,\ 0.70,\ 1.25,\ 2.50\}$$

$$L_y \in \{0.10\ 0.20,\ 0.40,\ 0.80,\ 1.50\},$$

respectively, in order to have different values of the sampling ratio $\kappa_x = 38/L_x$ and $\kappa_y = 38/L_y$, being 38 the number of mesh sides on $[0, r_{max}]$ for $\theta = 0$ in the considered mesh. The average mesh size $H = h = r_{max}/38 \approx 0.0625$. Convergence threshold on $\|\mathbf{u}-\mathbf{u}^{*,(k)}\|_2$ is set

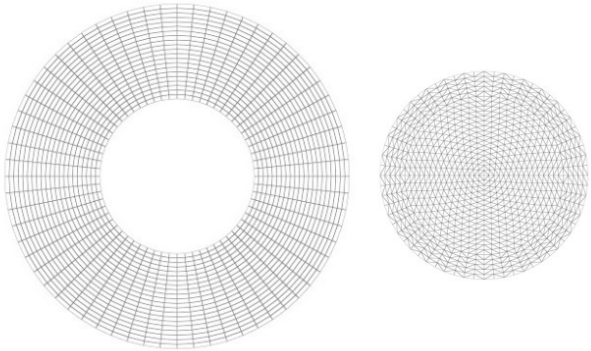

Figure 8 In Ω_H, a polar structured mesh of 21×64 curved elements (left) and in ω_h, an unstructured mesh of 1664 straight triangles (right).

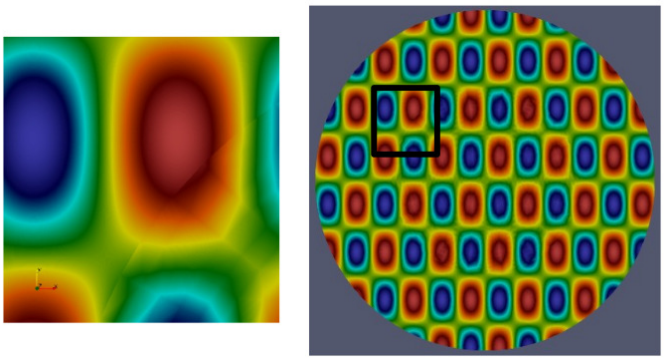

Figure 9 Computed rHCT-HB FE coupled solution in the whole domain $\Omega_H \cup \omega_h$ (right). A zoom (left) of the computed solution in a neighborhood of the overlapping area (delimited by the black box).

to 10^{-10} and the algorithm (17) converges in 21 iterations for all values of (L_x, L_y). Indeed, the overlap δ between Ω_H and ω_h is constant and equal to $5 \times h$. In Figure 10 (left), we report the logarithms of the norms $\|\mathbf{u}^{\square,(k)} - \mathbf{u}^{\square,(k-1)}\|_2$ (line with $+$) and $\|\mathbf{u}^{\triangle,(k)} - \mathbf{u}^{\triangle,(k-1)}\|_2$ (points x), for the last 12 (out of 21) iterations k of algorithm (17), of the coupled solution, for three values of L_x, respectively, 0.17 (the lowest lines/dots), 0.35 (the middle lines/dots), 1.25 (the highest lines/dots). The lines which fit the iteration residual norms have slopes -0.70, -0.94, -0.98, in Ω_H (and close values in ω_h), respectively, thus the convergence factor of the method is $-\ln(\rho(\mathcal{AB})) \approx 1$.

In Figure 10 (right) we report the infinite norm of the global errors $(u - u^*)$ and $\partial_x(u - u^*)$ for the coupled problem as a function of the inverse of κ_x. They both behave as the rHCT FE ones. We remark that when $L_x = 2.5$ (that means $\kappa_x \approx 15$), the error is important, whereas for $L_x = 0.35$ (that means $\kappa_x \approx 108$), we have many points per wavelength, thus a good precision on the solution.

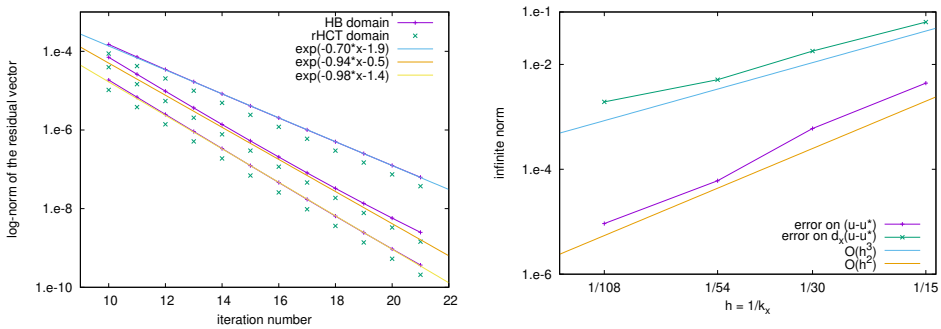

Figure 10 Log-norm of the residual vector along the iterations of the algorithm 17 to compute the rHCT-HB FE coupled solution shown in Fig. 9 (left). The line fitting the residuals in the HB domain. Global error as a function of the mesh size h in log scale (right).

6 | CONCLUSIONS

We have proposed and analyzed a non-conforming domain decomposition method which allows to couple two different FEs of class $\mathcal{C}^1$ on composite meshes. In plasma simulations, the $\mathcal{C}^1$ continuity is not enforced at particular points (such as the X-point or the plasma axis in a flux aligned grid) shared by more than four elements, making impossible to impose enough conditions that assure it. A special treatment in the neighborhood of these points is necessary (see an example [8]). In this work, we have relied on composite meshes to bypass this problem, namely, we stop the mesh of quadrangles before it becomes unstructured, and cover this small neighborhood of critical points by a mesh τ_h of triangles over which rHCT FEs are adopted. The two meshes τ_H, τ_h are then coupled by suitable operators, here based on interpolation. The global discrete problem is then solved iteratively, by an algorithm which can be straightforwardly introduced in already existing MHD codes, such as `JOREK` [3]. The possibility of using mortar like projections at the coupling interfaces $Gamma$, γ and isoparametric FEs also on the triangular mesh is left to further application as well as the simulation of a plasma equilibrium with this coupled approach.

ACKNOWLEDGMENTS

FR thanks INRIA for the delegation during which this work was accomplished. HG and BN have worked within the framework of the EURO Fusion Consortium. The views and opinions expressed herein do not necessarily reflect those of the European Commission.

Financial disclosure

FR is supported by the French National Research Agency grant SISTEM (ANR-19-CE46-0005-03). HG and BN have received funding from Euratom research and training programs 2014-2018, 2019-2020, under the grant agreement N.633053.

Conflict of interest

The authors declare no potential conflict of interests.

References

1. Blum J. Numerical Simulation and Optimal Control in Plasma Physics with Applications to Tokamaks. Series in Modern Applied MathematicsParis: Wiley Gauthier-Villars . 1989.

2. Faugeras B. An overview of the numerical methods for tokamak plasma equilibrium computation implemented in the NICE code. 2020; 160: 112020. https://doi.org/10.1016/j.fusengdes.2020.112020.

3. https://www.jorek.eu; 2020 (last accessed Feb. 29, 2020).

4. Czarny O, Huysmans G. Bézier surfaces and finite elements for MHD simulations. Journal of Computational Physics 2008; 227(16): 7423 - 7445. https://doi.org/10.1016/j.jcp.2008.04.001.

5. Hoelzl M, Huijsmans G, Pamela S, et al. The JOREK non-linear extended MHD code and applications to large-scale instabilities and their control in magnetically confined fusion plasmas. Nuclear Fusion 2021; 61(6): 065001. https://iopscience.iop.org/article/10.1088/1741-4326/abf99f.

6. http://www.iter.org/default.aspx; 2020 (last accessed Feb. 29, 2020).

7. Guillard H, Lakhlili J, Loseille A, et al. Tokamesh : A software for mesh generation in tokamaks. Research Report RR-9230, INRIA; 2018. https://hal.inria.fr/hal-01948060.

8. Bhole A, Nkonga B, Pamela S, Huijsmans G, Hoelzl M. Treatment of polar grid singularities in the bi-cubic Hermite-Bézier approximations: isoparametric finite element framework. Preprint, 2022. https://hal.archives-ouvertes.fr/hal-03781896.

9. Henshaw W, Brislawn K, Brown D, et al. An object-oriented framework for solving PDEs on overlapping grids. In: Los Alamos; 1996. https://www.osti.gov/servlets/purl/7809.

10. Clough R, Tocher J. Finite element stiffness matrices for analysis of plates in bending. In: ; 1965; Air Force Inst of Tech., Wright Patterson A.F Base, Ohio.

11. Ciarlet P. The Finite Element Method for Elliptic Problems. Amsterdam: North-Holland Publishing Co. . 1978. Studies in Mathematics and its Applications, Vol. 4.

12. Bernardou M, Hassan K. Basis functions for general Hsieh-Clough-Tocher triangles, complete or reduced. Research Report RR-0005, INRIA; 1980. https://hal.inria.fr/inria-00076556.

13. Elarif A, Faugeras B, Rapetti F. Tokamak free-boundary plasma equilibrium computation using finite elements of class C0 and C1 within a mortar element approach. 2021; 439: 110338. https://doi.org/10.1016/j.jcp.2021.110388.

14. Heumann H, Rapetti F. A finite element method with overlapping meshes for free-boundary axisymmetric plasma equilibria in realistic geometries. 2017; 334: 522-540. https://doi.org/10.1016/j.jcp.2017.01.006.

15. Smith B, Bjørstad P, Gropp W. Domain Decomposition. Parallel Multilevel Methods for Elliptic Partial Differential Equations. Cambridge University Press . 1996.

16. Achdou Y, Maday Y, Widlund O. Iterative Substructuring Preconditioners for Mortar Element Methods in Two Dimensions. SIAM J. Numer. Anal. 1999; 36: 551-580. https://doi.org/10.1137/S0036142997321005.

17. Cai XC, Dryja M, Sarkis M. Overlapping nonmatching grid mortar element methods for elliptic problems. SIAM J. Numer. Anal. 1999; 36(2): 581–606. http://dx.doi.org/10.1137/S0036142997323582doi: 10.1137/S0036142997323582

18. Hecht F, Lozinski A, Pironneau O. Numerical Zoom and the Schwarz Algorithm. In: Bercovier M, al. e., eds. Domain Decomposition Methods in Science and Engineering XVIII, LNCSE, Vol. 70Springer; 2009: 63-73. https://doi.org/10.1007/978-3-642-02677-5_6.

19. Ciarlet P. Discrete Maximum Principle for Finite-Difference Operators. Aequationes Mathematicae 1970; 4: 338-352. https://doi.org/10.1007/BF01844166.

20. Bernardi C, Maday Y, Patera A. A new nonconforming approach to domain decomposition: the Mortar element method. Brezis, H.(ed.) et al., Nonlinear partial differential equations and their applications. Collège de France Seminar, volume XI. Lectures presented at the weekly seminar on applied mathematics, Paris, France, 1989.

21. Achdou Y. The mortar element method with overlapping subdomains. SIAM J. Numer. Anal. 2002; 40: 601-628. https://doi.org/10.1137/S0036142900375256.

22. Marcinkowski L. Mortar methods for some second and fourth order elliptic equations. Institute of Applied Mathematics . 1999. Thesis (Ph.D.)–Warsaw University (Poland).

23. Raviart P, Thomas J. Introduction à l'analyse numérique des équations aux dérivées partielles. Paris: Masson . 1983.

How to cite this article: A. Bhole, H. Guillard, B. Nkonga, and F. Rapetti (2022), Coupling finite elements of class $\mathcal{C}^1$ on composite curved meshes for second order elliptic problems